Search for Spatially Extended *Fermi*-LAT Sources Using Two Years of Flight Data

J. Lande[2], S. Funk[2], M. Ackermann (???), . . .

ABSTRACT

Spatial extension is an important characteristic for correctly associating LAT sources with their counterparts at other wavelengths and for obtaining an unbiased model of their spectra. We present a new method for quantifying the spatial extension of sources with the Large Area Telescope (LAT), the primary science instrument on the *Fermi Gamma-ray Space Telescope* (*Fermi*). We perform a series of Monte Carlo simulations to validate this tool and calculate the LAT's threshold for detecting the spatial extension of sources. We then test all sources in the second *Fermi*-LAT catalog (2FGL) for extension. We report the detection of nine spatially extended sources in addition to the twelve spatially extended sources reported in 2FGL.

Subject headings: Catalogs; Fermi Gamma-ray Space Telescope; Gamma rays: observations; ISM: supernova remnants; Methods: statistical; pulsar wind nebula

1. Introduction

A number of astrophysical source classes including supernova remnants (SNRs), pulsar wind nebulae (PWNe), molecular clouds, normal galaxies, and galaxy clusters are expected to be spatially resolvable at GeV energies. Dark matter satellites are also hypothesized to be spatially extended. The Large Area Telescope (LAT) on the *Fermi Gamma-ray Space Telescope* (*Fermi*) has detected seven SNRs which are significantly extended at GeV energies: W51C, W30, IC443, W28, W44, RX J1713.7−3946, and the Cygnus Loop (Abdo et al. 2009b; Castro & Slane 2010; Abdo et al. 2010i,e,h, 2011c; Katagiri et al. 2011). In addition, three extended PWNe were detected as being extended: MSH 15−52, Vela X, and

[2]W. W. Hansen Experimental Physics Laboratory, Kavli Institute for Particle Astrophysics and Cosmology, Department of Physics and SLAC National Accelerator Laboratory, Stanford University, Stanford, CA 94305, USA

[53]Institut für Astronomie und Astrophysik, Universität Tübingen, D 72076 Tübingen, Germany

HESS J1825−137 (Abdo et al. 2010a,f; Grondin et al. 2011). Two close-by galaxies, the Large and Small Magalenic Clouds, and one radio galaxy, Centarus A, were spatially resolved at GeV energies (Abdo et al. 2010j,b,c). A number of additional sources detected at GeV energies are positionally coincident with sources that exhibit extension at other wavelengths, large enough to be spatially resolvable by the LAT at GeV energies.

The current generation of air Cherenkov detectors have made it apparent that many sources can be spatially resolved at even higher energies. Most prominent was a survey of the Galactic plane using the High Energy Stereoscopic System (H.E.S.S) which reported 14 spatially extended sources with extensions varying from $\sim 0°.1$ to $\sim 0°.25$ (Aharonian et al. 2006). In fact, within our Galaxy only very few sources detected at TeV energies (most notably the γ-ray binaries LS 5039 (Aharonian et al. 2006a), LS I+61−303 (Albert et al. 2006; Acciari et al. 2011), HESS J0632+057 (Aharonian et al. 2007c), and the Crab nebula (Weekes et al. 1989)) have no detectable extension. High-energy γ-rays from these sources originate by the decay of π^0s produced by hadronic interactions with interstellar matter and by relativistic electrons due to Inverse Compton (IC) scattering and Bremsstrahlung radiation (Blandford & Eichler 1987). It is likely that the GeV and TeV emission from these sources originates from the same population of high-energy particles and so at least some of these sources should be detected at GeV energies. Studying these TeV sources at GeV energies would help to determine the emission mechanisms producing these high energy photons.

The LAT is a pair conversion telescope that has been surveying the γ-ray sky since 2008 June. The LAT has broad energy coverage (20 MeV to > 300 GeV), wide field of view (~ 2.4 sr), and large effective area (~ 8000 cm^2 at > 1GeV). Using one year of all-sky surveying data, the LAT Collaboration published a catalog of 1451 sources significantly detected at GeV energies called 1FGL (Abdo et al. 2010d). Using two years of data, a second catalog called 2FGL reported on 1873 sources (Abdo et al. 2011b). The counterparts of many of these sources can be spatially resolved when observed at other frequencies but detecting the spatial extension of these sources at GeV energies is difficult because the size of the point-spread function (PSF) of the LAT is comparable to the typical size of many of these sources.

The capability to spatially resolve GeV γ-ray sources is important for several reasons. Finding a coherent source extension across different energy bands can help to associate a LAT source to an otherwise confused counterpart. Furthermore, some of the dark matter substructure in our Galaxy is predicted to be spatially extended at GeV energies (Baltz et al. 2008). Characterization of spatial extension could help to identify this substructure. Also, due to the strong energy dependence of the LAT PSF, the spatial and spectral character of

a source do not decouple. An inaccurate spatial model will bias the spectral model of the source and vice versa. Specifically, modeling a spatially extended source as point-like will systematically shift a spectral analysis to softer indices. Furthermore, correctly modeling a source's extension is important for understanding an entire region of the sky. For example, an incorrect model of the spatially extended LMC introduced significant residuals in the surrounding region (Abdo et al. 2010d, 2011b). Such residuals can bias the significance and measured spectrum of neighboring sources in the densely populated Galactic plane.

Previous analysis of extended LAT sources were performed as dedicated studies of individual sources, so we expect that a systematic scan of all LAT detected sources could uncover additional spatially extended sources. For these reasons, in Section 2 we present a new systematic method for analyzing spatially extended LAT sources. In Section 3, we demonstrate that this method can be used to test the statistical significance of the extension of a LAT sources and in Section 4 we calculate the LAT's detection threshold to resolve the extension of a source. In Section 5, we describe a search for new spatially extended LAT sources and in Section 6 we reanalyze the twelve previously detected extended sources included in 2FGL. In Section 7 we further demonstrate that our detection method does not misidentify point-like sources as being extended by testing the extension of active galactic nuclei (AGN) believed to be unresolvable. Finally, in Section 8 we present the detection of the extension of nine spatially extended sources that were reported in 2FGL but not previously spatially resolved.

2. Analysis Methods

Morphological studies of sources using the LAT are challenging because of the strongly energy-dependent PSF that is comparable in size to the extension of many sources expected to be detected at GeV energies. Additional complications arise for sources along the Galactic plane due to systematic uncertainties in the Galactic diffuse emission. The LAT's PSF is limited at its lowest detectable energies by multiple scattering in the silicon strip tracking section of the detector and is several degrees at 100 MeV. The PSF improves with energy approaching a 68% containment radius of $\sim 0°.2$ at the highest energies (when averaged over the acceptance of the LAT) and is limited by the granularity of the silicon strips in the tracker (Atwood et al. 2009; Abdo et al. 2009e, 2011a).[1] However, since most high energy astrophysical sources have spectra that decrease rapidly with increasing energy, the improved resolution of the higher energy photons is typically offset by their low statistics. Therefore

---

[1]More information about the performance of the LAT can be found at the *Fermi* Science Support Center (FSSC, http://fermi.gsfc.nasa.gov).

84 sophisticated analysis techniques are required to maximize the LATs sensitivity to these
85 extended sources.

2.1. The `pointlike` Package

87   A new analysis tool has been developed to address the unique requirements for study-
88 ing spatially extended sources with the LAT. The Poisson likelihood to find the observing
89 counts is maximized given a parametrized spatial and spectral model of the source and its
90 surrounding region. The sky is divided into cubes of space and energy using the healpix
91 representation of the sky (Górski et al. 2005) and the likelihood is maximized over all bins
92 in a region. The extension of a source can be modeled by a geometric shape (e.g. a disk
93 or a two-dimensional Gaussian) and the source's position, extension, and spectrum can be
94 simultaneously fit.

95   This type of analysis is not feasible using the standard LAT likelihood analysis tool
96 `gtlike` [2] because it can only fit the spectral parameters of the model unless a more so-
97 phisticated iterative procedure is used to also test various source morphologies. We note
98 that `gtlike` has been used in the past in several studies of source extension in the LAT
99 Collaboration (Abdo et al. 2010j,b,e, 2009b). In these studies, a profile based upon a set
100 of `gtlike` maximum likelihood fits at fixed extensions was used to build a profile of the
101 likelihood as a function of extension. This approach is not optimal because the position,
102 extension, and spectrum of the source must be simultaneously fit to find the best fit param-
103 eters and to correctly compute the statistical significance of a detection. Furthermore since
104 the `gtlike` likelihood profile approach is computationally intensive, no large-scale Monte
105 Carlo simulations have been run to validate it.

106   The approach presented here is based on a second maximum likelihood fitting package
107 developed in the LAT Collaboration called `pointlike` (Abdo et al. 2010d; Kerr 2011). The
108 choice to base the spatial extension fitting on `pointlike` rather than `gtlike` was made on
109 considerations of computing time. The `pointlike` algorithm was optimized for speed to
110 handle larger numbers of sources efficiently which is important for our catalog scan and
111 for being able to perform large-scale Monte Carlo simulations to validate the analysis. De-
112 tails on the `pointlike` package can be found in Kerr (2011). We extended the code to
113 allow a simultaneous fit of the source extension together with the position and the spectral
114 parameters.

---

[2]`gtlike` is distributed publicly by the FSSC.

2.2. Extension Fitting

In `pointlike`, it is assumed that the spatial and spectral model of an extended source are separable, i.e. that the source model $M(l, b, E) = S(l, b) \times X(E)$ where $S(l, b)$ is the spatial distribution and $X(E)$ is the spectral distribution. To fit an extended source, `pointlike` convolves the extended source shape with the PSF (as a function of energy) and uses the `minuit` library (James & Roos 1975) to maximize the likelihood by simultaneously varying the position, extension, and spectrum of the source. As will be described in Section 3, simultaneously fitting the position, extension, and spectrum is important to correctly calculate the statistical significance of the detection of extension of a source. To avoid projection effects, the source's longitude and latitude are not directly fit but instead the source's displacement in a rotated reference frame.

The significance of the extension of a source can be calculated from the likelihood ratio test of a hypothesis with a spatially extended source and a hypothesis with a point-like source. The test statistic for this procedure is defined as

$$\mathrm{TS_{ext}} = 2 \log(\mathcal{L}_{\mathrm{ext}} / \mathcal{L}_{\mathrm{ps}}) \tag{1}$$

where $\mathcal{L}$ is the Poisson likelihood. `pointlike` calculates $\mathrm{TS_{ext}}$ by fitting a source first with a spatially extended model and then as a point-like source. The interpretation of $\mathrm{TS_{ext}}$ in terms of a statistical significance is discussed in Section 3.

For extended sources with an assumed radially symmetric shape, we optimized the calculation by performing one of the integrals analytically. The expected photon distribution can be written as

$$\mathrm{PDF}(\vec{r}) = \int \mathrm{PSF}(|\vec{r} - \vec{r'}|) I_{\mathrm{src}}(\vec{r'}) r' dr' d\phi' \tag{2}$$

For the LAT, the PSF can be parameterized by a King function (King 1962):

$$\mathrm{PSF}(r) = \frac{1}{2\pi\sigma^2} \left(1 - \frac{1}{\gamma}\right) \left(1 + \frac{u}{\gamma}\right)^{-\gamma}, \tag{3}$$

where $u = (r/\sigma)^2/2$ and σ and γ are free parameters (Kerr 2011). For radially symmetric extended sources, the angular part of the integral can be evaluated analytically

$$\mathrm{PDF}(u) = \int_0^\infty r' dr' I_{\mathrm{src}}(v) \int_0^{2\pi} d\phi' \mathrm{PSF}(\sqrt{2\sigma^2(u + v - 2\sqrt{uv}\cos(\phi - \phi'))}) \tag{4}$$

$$= \int_0^\infty dv I_{\mathrm{src}}(v) \left(\frac{\gamma - 1}{\gamma}\right) \left(\frac{\gamma}{\gamma + u + v}\right)^\gamma \times {}_2F_1\left(\gamma/2, \frac{1+\gamma}{2}, 1, \frac{4uv}{(\gamma + u + v)^2}\right). \tag{5}$$

where $v = (r'/\sigma)^2/2$ and ${}_2F_1$ is the Gaussian hypergeometric function. This convolution formula reduces the expected photon distribution to a single numerical integral.

There will always be a small numerical discrepancy between the expected photon distribution derived from a true point-like source and a very small extended source due to numerical error in the convolution. In most situations, this error is insignificant. But in particular for very bright sources, this numerical error has the potential to bias the test statistic for the extension test. Therefore, when calculating TS_{ext}, we compare the likelihood fitting the source with an extended spatial model to the likelihood when fixing its extension to $10^{-10 \circ}$.

We estimate the error on the extension of a source by fixing the position of the source and varying the extension until the likelihood has fallen by $\frac{1}{2}$, corresponding to a 1σ error (Eadie et al. 1971). Figure 1 demonstrates this method by showing the change in the log of the likelihood when varying the extension of the SNR IC443. The localization error is calculated by fixing the extension and spectrum of the source and fitting to the likelihood function a 2D Gaussian as a function of position.

2.3. `gtlike` Analysis Validation

`pointlike` is important for LAT analyses that require many iterations such as source localization and extension fitting. On the other hand, because `gtlike` makes fewer approximations in calculating the likelihood we expect the spectral parameters found with `gtlike` to be slightly more precise. Furthermore, because `gtlike` is the standard likelihood analysis package, it has been more extensively validated for spectral analysis. For those reasons, in the following analysis we used `pointlike` to determine the position and extension of a source and subsequently derived the spectrum using `gtlike`. Both `gtlike` and `pointlike` can be used to estimate the statistical significance of the extension of a source and we required that both methods agree for a source to be considered extended. There was good agreement between the two methods. Unless explicitly mentioned, all TS, TS_{ext}, and spectral parameters were calculated using `gtlike` with the best-fit positions and extension found by `pointlike`.

2.4. Dual Localization

There is a degeneracy between a spatially extended source and multiple point-like sources separated by angular distances comparable to or smaller than the size of the LAT PSF. To assess the possibility of source confusion, we use `pointlike` to simultaneously fit the position of two point-like sources in the region of extended source candidates.

We define TS_{inc} as twice the increase in the log of the likelihood fitting the region as

two point-like sources compared to fitting the region as one point-like source:

$$\mathrm{TS_{inc}} = 2\log(\mathcal{L}_{2\mathrm{pts}}/\mathcal{L}_{\mathrm{ps}}). \tag{6}$$

$\mathrm{TS_{inc}}$ can not be directly compared to $\mathrm{TS_{ext}}$ to see which model is more significant because the models are not nested (Protassov et al. 2002). Even though the comparison of $\mathrm{TS_{ext}}$ with $\mathrm{TS_{inc}}$ is not a calibrated test, we find the cases $\mathrm{TS_{inc}} \ll \mathrm{TS_{ext}}$ and $\mathrm{TS_{inc}} \gg \mathrm{TS_{ext}}$ suggestive and we only consider a source to be extended if $\mathrm{TS_{ext}} > \mathrm{TS_{inc}}$. Similar to the case of extended sources described in Section 2.3, the spectra of the two point-like sources can be refit using `gtlike`. We quote the spectral values obtained from `gtlike` using the best fit positions found using `pointlike`.

2.5. Comparing Source Sizes

We tested two different models for the surface brightness profile, either a 2D Gaussian

$$I(x, y) = \tfrac{1}{2\pi\sigma^2} \exp\left(-(x^2 + y^2)/2\sigma^2\right) \tag{7}$$

or a uniform surface brightness

$$I(x, y) = \begin{cases} \frac{1}{\pi\sigma^2} & x^2 + y^2 \leq \sigma^2 \\ 0 & x^2 + y^2 > \sigma^2. \end{cases} \tag{8}$$

Although these shapes are significantly different, Figure 2 shows the their PDF are very similar for an example source of size $0°.5$.[3] The LAT has little sensitivity /thereto the exact structure of extended source. Therefore, in our search for extended sources we used only a uniform surface brightness as our spatial extension shape. We quote the radius of the edge (σ) as the size of the source.

3. Validation of Analysis Method

We test the false detection probability of for the extended source test by fitting the extension of point-like sources. Mattox et al. (1996) discuss that the test statistic distribution for a likelihood ratio test on the existence of a source at a given position is

$$P(\mathrm{TS}) = \tfrac{1}{2}(\chi_1^2(\mathrm{TS}) + \delta(\mathrm{TS})). \tag{9}$$

---

[3]To allow a valid comparison between the Gaussian and the uniform surface brightness morphologies, we define here the source size $(0°.5)$ as the radius containing 68% of the intensity $(\mathrm{r_{68}})$. $\mathrm{r_{68,Gaussian}} = 1.51\sigma$ and $\mathrm{r_{68,disk}} = 0.82\sigma$ where σ is defined in Equation 7 and Equation 8 respectively.

175 The particular form of Equation 9 is due to the null hypothesis (source flux $\Phi = 0$) residing
176 on the edge of parameter space and the model hypothesis adding a single degree of freedom
177 and leads to the often quoted result that the square root of the test statistic is the number of
178 σ of the detection. It is plausible to expect a similar distribution of the test statistic in the
179 test for source extension since the same conditions apply (with the source flux Φ replaced
180 by the source radius r and $r < 0$ being unphysical). We performed Monte Carlo simulations
181 to calculate empirical distributions for $\mathrm{TS_{ext}}$ and we compared them to Equation 9.

182 We simulated point-like sources with various spectral forms using the LAT on-orbit
183 simulation tool `gtobssim` [4] and fit the sources with `pointlike` using both point-like and ex-
184 tended source hypotheses. These point-like sources were simulated with a power-law spectral
185 model with integrated fluxes above 100 MeV ranging from 3×10^{-9} to 1×10^{-6} ph cm^{-2} s^{-1}
186 in six discrete steps and spectral indices ranging from 1.5 to 3 in four discrete steps. These
187 values were picked to represent typical source parameters of LAT-detected sources. The
188 point-like sources were simulated on top of an isotropic background with an integrated flux
189 above 100 MeV of 1.5×10^{-5} ph cm^{-2} s^{-1} taken to be the same as the isotropic spectrum
190 measured by EGRET (Sreekumar et al. 1998). The Monte Carlo simulation was performed
191 over a one-year observation period using a representative rocking profile and a representative
192 livetime fraction of 0.8. The reconstruction was performed using photons with energies be-
193 tween 1 GeV and 100 GeV and the Pass 7_V6 (P7_V6) Source Instrument Response Function
194 (IRFs, Abdo et al. (2011a)). For each significantly detected point-like source (TS $\geq$ 25), we
195 used `pointlike` to fit the source as an extended source and calculate $\mathrm{TS_{ext}}$.

196 For each set of spectral parameters, $\sim 30,000$ statistically independent simulations were
197 performed. For dimmer spectral models, many of the simulations left the source undetected
198 (TS < 25) and were discarded. Table 1 shows the different spectral models used in our study
199 as well as the number of simulations and the average point-like source significance. The
200 cumulative density of $\mathrm{TS_{ext}}$ is plotted in Figure 3 and compared to the $\chi^2_1/2$ distribution of
201 Equation 9.

202 Our study shows broad agreement between simulations and Equation 9. Nevertheless,
203 the agreement is not perfect. It should be noted that the discrepancy seems to be worst for
204 bright sources where numerical errors in the convolution are most apparent. Another possible
205 reason for the departure from Equation 9 is that `pointlike` ignores energy dispersion which
206 will change the PSF shape as a function of energy. We emphasize that many of the empirical
207 distributions lie to the left of the theoretical curve so using the theoretical distribution will
208 often lead to an underestimate of the statistical significance of a detection. Therefore, we

---

[4]`gtobssim` is distributed publicly by the FSSC.

209 are confident that $\mathrm{TS_{ext}}$ can be used as a conservative measure of the statistical significance
210 of a source's extension and we used it in the following analysis.

4. Extended Source Detection Threshold

212   We calculated the LAT's threshold to detect that a spatially extended source is extended.
213 We define the detection threshold as the flux at which the value of $\mathrm{TS_{ext}}$ averaged over many
214 statistical realizations of a source is $\langle \mathrm{TS_{ext}} \rangle = 16$, corresponding to a 4σ detection.

215   We used a simulation setup similar to that described in Section 3, but instead of point-
216 like sources we simulated extended sources with a radially symmetric uniform surface bright-
217 ness. Additionally, we simulated our sources over the two-year time range included in 2FGL.
218 For each extension and spectral index, we selected a flux range which bracketed $\mathrm{TS_{ext}} = 16$
219 and performed an extension test for > 100 independent realizations of ten fluxes in the range.
220 We calculated $\langle \mathrm{TS_{ext}} \rangle = 16$ by fitting a line to the flux and $\mathrm{TS_{ext}}$ values in the narrow range.

221   Figure 4 shows the threshold for sources of four spectral indices from 1.5 to 3 and
222 extensions varying from $\sigma = 0°.1$ to $2°.0$. The LAT's flux threshold for a significant detection
223 of source extension drops quickly with increasing source size and reaches a minimum around
224 $0°.5$. Figure 4 shows the threshold using photons with energies between 100 MeV and 100 GeV
225 and also using only photons with energies between 1 GeV and 100 GeV. Except for very large
226 ($> 1°$) sources, our detection threshold is not substantially improved by including photons
227 with energies between 100 MeV and 1 GeV. This is also demonstrated in Figure 1 which
228 shows $\mathrm{TS_{ext}}$ for the SNR IC443 computed independently in twelve energy bins between 100
229 MeV and 100 GeV. For IC443, which has a spectral index ~ 2.4, almost the entire increase
230 in likelihood modeling the source as being extended comes from energies above 1 GeV. On
231 the other hand, other systematic errors become increasingly important at low energy. For
232 our extension search, we therefore used only photons with energies above 1 GeV.

233   Figure 5 shows the flux threshold as a function of source extension for different back-
234 ground levels ($1\times$, $10\times$, and $100\times$ the nominal background), different spectral indices, and
235 two different energy ranges (1 GeV to 100 GeV and 10 GeV to 100 GeV). The detection
236 threshold is higher for sources in regions of higher background. When studying sources only
237 at energies above 1 GeV, the LAT's detection threshold (defined as the 1 GeV to 100 GeV
238 flux at which $\langle \mathrm{TS_{ext}} \rangle = 16$) depends less strongly on the source's spectral index. The index
239 dependence of the detection threshold is even weaker when considering only photons with
240 energies above 10 GeV. Overlaid on Figure 5 are the LAT detected extended sources that
241 will be discussed in Sections 6 and 8. The extension thresholds are tabulated in Table 2.

Finally, Figure 6 shows the LAT's projected detection threshold to extension with a 10 year exposure against 10 times the isotropic background. This background is representative of the background near the Galactic plane. For small extended sources, our detection threshold improves by a factor larger than the square root of the exposure because at high energies, where we are most sensitive to extension, the background levels are in the Poisson instead of the Gaussian regime. For large extended sources, the relevant background is over a larger spatial range and so the improvement is closer to the expected factor corresponding to the square root of the exposure.

5.   Extended Source Search Method

We tested all sources in 2FGL for spatial extension. 2FGL included twelve previously published spatially extended sources but not attempt was made to fit the extension of these sources. Other than these sources, all 2FGL sources were modeled as point-like and 2FGL did no attempt to resolve their extension.

Our analysis technique is closely related to that of the 2FGL catalog. We used the same two-year dataset from 2008 August 4 to 2010 August 1 and we used the same P7_V6 Source class event selection and IRFs (Abdo et al. 2011a). The same models were used to describe the background from Galactic diffuse, isotropic, and Earth limb emission. To account for possible residuals in the diffuse emission model, the galactic emission was scaled by a power-law and the isotropic component's normalization was left free.

As was shown in Section 4, we gain little in sensitivity using photons with energies below 1 GeV. On the other hand, the large PSF at low energy makes us more susceptible to systematic errors arising from source confusion due to multiple point-like sources and modeling of the Galactic diffuse emission. In addition, the Galactic diffuse emission is more pronounced at lower energies due to its steep energy spectrum (Abdo et al. 2009a). For that reason, we performed our search using only photons with energies between 1 GeV and 100 GeV.

We also performed a search for extended sources using only photons with energies between 10 GeV and 100 GeV. Although this approach tests the same sources, it is complimentary because the Galactic diffuse emission is even less dominant above 10 GeV. Furthermore, source confusion becomes less of a problem since most LAT sources are not significantly detected at energies exclusively above 10 GeV. So we expect to be able to resolve harder sources in more complicated regions by restricting our analysis to higher energies. The > 10 GeV analysis is especially beneficial for regions near pulsars which are not significantly detected

above 10 GeV. A similar procedure was used to detect HESS J1825−137 and MSH 15−52 with the LAT (Abdo et al. 2010a; Grondin et al. 2011).

We tested each source for extension using `pointlike` assuming the source had a uniform radially symmetric surface brightness and a power-law spectral model. We used a circular 10° region of interest (ROI) centered on our source and included all catalog sources within 15° of the source of interest in our background model. We refit the spectral parameters of sources within 2° of the source to avoid potential biases of the extension parameters of the source of interest due to close-by background sources.

Finally, when analyzing each region, we automatically removed from our background model other 2FGL sources which were within 0°.5 of the source of interest. This was done due to a concern that extended sources could be included in 2FGL as multiple point-like sources. These spurious sources could distort the extension fit. Instead, when a source was found to be significantly extended (i.e. $TS_{ext} > 16$), we performed the dual localization procedure to compare the extended source hypothesis to the hypothesis of two independent point-like sources (section 2.4). Only sources with $TS_{ext} > TS_{inc}$ were considered as extended.

5.1. Additional Analysis

We expect most spatially resolvable extended sources to be located in our Galaxy and thus to be concentrated along the Galactic plane. Unfortunately, the GeV emission in the Galactic plane is dominated by extremely structured diffuse emission from the interactions of cosmic rays with the interstellar medium. Finding sources on top of this emission is difficult as was discussed in 1FGL and 2FGL (Abdo et al. 2010d, 2011b). Furthermore, the Galactic plane is crowded and it is often difficult to correctly model nearby sources. Because of this, finding a source with $TS_{ext} > 16$ is not a sufficient criteria alone for claiming the detection of source extension. For each extended source, we perform several analysis crosschecks.

For each candidate, we generated a map of residual TS by adding a new source of spectral index 2 into the region at each pixel and finding the increase in likelihood when fitting its flux. Figure 7 shows a residual TS map for the extended source IC443. The residual TS map indicates that the spatially extended model for IC443 is a significantly better description of the observed photons and that there is no significant residual in region after modeling the source as being spatially extended. We also generated maps of the sum of all counts within a given distance of the source and compared it to the model predictions of a point-like source. An example radial integral plot is shown for the extended source IC443 in Figure 1. For each source, we also made diffuse-emission-subtracted smoothed counts maps (show for IC443 in

Figure 1).

We inspected each extended source candidate to identify cases in which the fit was influenced by large-scale residuals in the diffuse emission and hence the extension measurement was unreliable. An example of such a case is 2FGL J1856.2+0450c shown in Figure 8. The diffuse-emission-subtracted smoothed counts map shows that there appears to be large-scale residual in the diffuse emission in this region along the Galactic plane. As a result, 2FGL J1856.2+0450c is fit to an extension of $\sim 2°$ and the result is statistically significant with $TS_{ext} = 45.4$. However, by looking at the residuals it is clear that this complicated region is not fit well. We did not report as extended sources that fail this inspection.

For the remaining candidates, we took the extended source's spatial and spectral model found using `pointlike` and re-determined the spectral parameters using `gtlike`. We used the 'binned likelihood' mode of `gtlike` on a $14° \times 14°$ ROI with a pixel size of $0°.03$. We obtained a second measure of TS_{ext} from `gtlike` using the extension and position of the source as determined by `pointlike`. We only considered a source to be significantly extended if $TS_{ext} > 16$ with both `pointlike` and `gtlike`.

Because of the high source density in the Galactic plane, we often had to iteratively improve the model of our background sources to obtain a better fit of the candidate source. Several point-like 2FGL sources were often include in the catalog to fill in the emission of the extended source candidate and had to be removed from the background model of the region. Similarly, background sources were often insignificant at higher energies and had to be removed from the sky model. The position of background sources would often have to be refit once the extended source's extension was modeled. When the model of the extended source coupled strongly with nearby sources, we iteratively fit the extended source and all nearby sources until the fit converged. For each extended source, we describe any modifications required of the background model compared to 2FGL sky model.

5.2. Systematic Errors on Extension

We estimated a systematic error on the extension of a source due to uncertainty in our knowledge of the LAT PSF. Before launch, the LAT PSF was determined by detector simulations which were verified in accelerator tests (Atwood et al. 2009). However, in-flight data revealed a discrepancy above a few GeV in the PSF compared to the angular distribution of photons from bright AGN (Abdo et al. 2011a). Subsequently, the PSF was fit empirically to bright AGN and this empirical parameterization is used in the P7_V6 IRFs. To account for our uncertainty in our knowledge of the PSF, we refit our extended source candidates

using the pre-flight Monte Carlo representation of the PSF and consider the difference in extension found using the two PSFs as a systematic error on the extension of a source. The same approach was used in Abdo et al. (2010i). At high energies, we believe that our parameterization of the PSF from bright AGN is substantially better than the Monte Carlo representation of the PSF so this systematic error is conservative.

We estimate a second systematic error on the extension of a source due to uncertainty in out model of the Galactic diffuse emission by using an alternative diffuse model based upon GALPROP[5] and used in the LAT analysis of the isotropic diffuse emission (Abdo et al. 2010k). The intensities of various components of the Galactic diffuse emission were fitted individually using a spatial distribution of the intensities within the ROI as predicted by the model. We distinguished contributions from CR interactions with the molecular hydrogen, the atomic+ionized hydrogen, residual gas traced by dust (Grenier et al. 2005), and the interstellar radiation field. We further split the contributions from interactions with molecular and atomic hydrogen to the Galactic diffuse emission according to the distance from the Galactic center in which they are produced. Hence, we replaced the standard diffuse emission model by 18 individually fitted templates to describe individual components of the diffuse emission. A similar crosscheck was used in the LAT Collaboration's analysis of RX J1713.7−3946 (Abdo et al. 2011c).

It is not expected that this diffuse model is superior to the standard LAT model obtained through an all-sky fit. However, adding degrees of freedom to the background model can remove likely spurious sources that correlate with features in the Galactic diffuse emission. Therefore, this tests systematics that may be due to incorrect modeling of the diffuse emission in the region. We do not except the systematic error due to uncertainties in the PSF to be correlated to the systematic error due to uncertainty in the Galactic diffuse emission. Therefore, the total systematic error on the extension of a source was obtained by adding the two errors in quadrature.

6. Analysis of Extended Sources Identified in 2FGL

We first present on our analysis of the twelve extended sources included in 2FGL. (Abdo et al. 2011b). Six extended SNRs were included in 2FGL: W51C, IC443, W28, W30,

---

[5]GALPROP is a software package for calculating the Galactic γ-ray emission based on a model of cosmic-ray propagation in the Galaxy. See http://galprop.stanford.edu/ for details and references.

W44, and the Cygnus Loop (Abdo et al. 2009b, 2010i,e,h; Katagiri et al. 2011).[6] Using photons with energies between 1 GeV and 100 GeV, our analysis significantly detected the extension of all six SNRs.

Two nearby satellite galaxies of the Milky Way the Large Magalenic Cloud (LMC) and the Small Magalenic Cloud (SMC) were included in 2FGL as spatially extended sources (Abdo et al. 2010j,b). They were significantly detected using photons with energies between 1 GeV and 100 GeV. Our fit extension is comparable to the published result, but we note that the previous LAT Collaboration publication on LMC used a more complicated two 2D Gaussian surface brightness spatial model when fitting it ((Abdo et al. 2010j)).

Three PWNe, MSH 15−52, Vela X, and HESS J1825−137 were identified in 2FGL (Abdo et al. 2010a,f; Grondin et al. 2011). HESS J1825−137 was significantly detected using photons with energies between 10 GeV and 100 GeV. To improve our analysis of this source, we had to remove from our background model 2FGL J1823.1−1338c which was included in 2FGL to represent part of the extended emission. To avoid confusion with the nearby bright pulsar PSR J1509−5850, MSH 15−52 had to be analyzed at high energies. Using photons with energies above 10 GeV, we fit the extension of MSH 15−52 to be consistent with the published size but with an extension significance of $TS_{ext} = 6.5$.

Our analysis was unable to resolve Vela X which would have required first removing the pulsed photons from the Vela pulsar which was beyond the scope of this paper. Our analysis also failed to detect a significant extension for the Centaurus A Lobes because the source's emission is significantly different from a uniform radially symmetric surface brightness (Abdo et al. 2010c).

Our analysis of these sources is summarized in Table 3. This table includes the best fit position and extension of these sources when fitting them with a radially symmetric uniform surface brightness spatial model. It also includes the best fit spectral parameters for each source. The position and extension of Vela X and the Centaurus A Lobes were taken from Abdo et al. (2010f,c) and are included in this list for completeness.

7.   Test of 2LAC Sources

To validate our method, we tested LAT sources associated with AGN for extension. GeV emission from AGN is believed to originate from the cores of kiloparsec-scale jets of

---

[6]A detailed publication by the LAT Collaboration about W30 is in preparation. GeV emission from W30 was also studied in Castro & Slane (2010).

distant galaxies. Therefore AGN are not expected to be spatially resolvable by the LAT and provide a good calibration source to demonstrate that our extension detection method does not misidentify point-like sources as being extended. We note that megaparsec-scale γ-ray halos around AGNs have been hypothesized to be resolvable by the LAT (Aharonian et al. 1994). However, no such halo has been discovered in the LAT data so far.

Following 1FGL, the LAT Collaboration published the First LAT AGN Catalog (1LAC), a list of sources that had a high probability association with AGN (Abdo et al. 2010l). 1LAC associated 709 1FGL sources with 671 AGN at high latitude ($|b| > 10°$). Using two years of data and 2FGL, the Second LAT AGN Catalog (2LAC) associated 1016 2FGL sources with AGN (Ackermann et al. 2011). To avoid systematic problems with AGN classification, we selected only the 885 AGN which made it into the clean AGN sub-sample. An AGN association is considered clean only if it has a high probability of association $P \geq 80\%$, if it is the only AGN associated with the catalog source, and if there are no flags on the source in 2FGL. These last two conditions are important for our analysis. Source confusion may look like a spatially extended source and flagged catalog sources may correlate with unmodeled structure in the diffuse emission.

Of the 885 clean AGN, we selected the 783 of these 2FGL sources which were significantly-detected above 1 GeV and fit each of them for extension. The cumulative density of $\mathrm{TS}_{\mathrm{ext}}$ for these AGN compared to the $\chi^2/2$ distribution of Equation 9 is shown in Figure 9. The $\mathrm{TS}_{\mathrm{ext}}$ distribution for AGN shows good agreement with the theoretical distribution, but two sources had $\mathrm{TS}_{\mathrm{ext}} > 10$. One was due to the incorrect removal of a nearby catalog sources from the sky model (see Section 5) and the other was due to a failure of convergence of the point-like source hypothesis. This result demonstrates that we can use $\mathrm{TS}_{\mathrm{ext}}$ as a measure of the statistical significance of the detection of the extension of a source.

We should clarify that the LAT PSF used in this study was determined empirically by fitting the observed shape of bright AGN (see Section 5.2). Finding that the AGN we test are not extended is not surprising. This validation analysis is not suitable to reject any hypotheses about the existence of megaparsec-scale halos around AGN.

8.   New Extended Sources

Nine extended sources not included in 2FGL were found by our extended source search. Three were found when using photons with energies between 1 GeV and 100 GeV and six were found when using photons with energies between 10 GeV and 100 GeV. The spectral and spatial properties of these nine sources is summarized in Table 4. The results of our

investigation of systematic errors are presented in Table 5. it compares the fit extension with an extended source hypothesis to the fit assuming the emission originates from two independent point-like sources. For these extended extended sources, $TS_{ext} > TS_{inc}$ suggesting that the GeV emission does not originate from multiple physically distinct sources. Table 5 also includes the results of the extension fit using variations of the PSF and the galactic diffuse model described in Section 5.2. There is good agreement between TS_{ext} and the fit size using the standard analysis, the alternative diffuse models, and the alternative PSF. This suggests that the sources are robust against features in the diffuse emission model and uncertainties in the angular resolution of the LAT.

8.1. 2FGL J0823.0−4246

2FGL J0823.0−4246 was found to have an extension of $0°.37\pm0°.03_{stat}\pm0°.02_{sys}$ with an extension significance of $TS_{ext} = 46.3$ using photons with energies between 1 GeV and 100 GeV. This source was fit to $(l, b) = (260°.32, -3°.28)$ and is coincident with 1FGL J0823.3−4248. Figure 10 shows a counts map of this source and Figure 11 shows its spectrum. To get a good fit of this source, we had to remove from our background model the nearby sources 2FGL J0823.4−4305 and 2FGL J0821.0−4254 which were included in 2FGL to represent part of the extended emission.

This extended source is spatially coincident with the middle-aged SNR Puppis A. Puppis A has been studied in detail in radio (Castelletti et al. (2006), and references therein) and X-ray (Petre et al. (1996); Hwang et al. (2008), and references therein) Mosaic *ROSAT* observations of Puppis A produced the highest resolution X-ray image of this source and contours corresponding to this image are overlaid on Figure 10 and match the inferred size at GeV energies (Petre et al. 1996). Puppis A's distance was estimated at 2.2 kpc (Reynoso et al. 1995, 2003) and leads to a 1 GeV to 100 GeV luminosity of $\sim 3 \times 10^{34}$ ergs s^{-1}. No molecular clouds have been observed directly adjacent to Puppis A (Paron et al. 2008), similar to the LAT detected Cyngus Loop SNR (Katagiri et al. 2011). The luminosity of Puppis A is also smaller than that of other SNRs believed to interact with molecular clouds (Abdo et al. 2009b, 2010i,h,e,g).

8.2. 2FGL J1627.0−2425c

2FGL J1627.0−2425c was found to have an extension of $0°.41 \pm 0°.05_{stat} \pm 0°.02_{sys}$ with an extension significance of $TS_{ext} = 31.1$ using photons with energies between 1 GeV and 100

GeV. The source was fit to $(l, b) = (353°08, 16°78)$ and is coincident with 1FGL J1628.6−2419c. Figure 12 shows a counts map of this source.

This source is in a region of remarkably complicated diffuse emission. Even though it is 16° from the Galactic plane, this source is on top of the core of the Ophiuchus molecular cloud which contains massive star-forming regions that are bright in the infrared. The region also has abundant molecular and atomic gas traced by CO and HI but also plenty of dark gas found only by its association with dust emission (Grenier et al. 2005). Embedded star-forming regions make it even more challenging to measure the column density of dust. Infared and ^{12}CO $(J = 1 \rightarrow 0)$ contours are overlaid on Figure 12 and show good spatial correlation with the GeV emission (Young et al. 1986; de Geus et al. 1990). This source might represent γ-ray emission from the interactions of cosmic rays with interstellar gas which has not been accounted for in the LAT diffuse emission model.

8.3. 2FGL J1712.4−3941

2FGL J1712.4−3941 was found to have an extension $0°56 \pm 0°04_{\text{stat}} \pm 0°02_{\text{sys}}$ with an extension significance of $\text{TS}_{\text{ext}} = 39.6$ using photons with energies between 1 GeV and 100 GeV. This source was fit to $(l, b) = (347°25, -0°54)$ and is coincident with 1FGL J1711.7−3944c. Figure 13 shows a counts map of this source. This source is spatially coincident with the SNR RX J1713.7−3946 and was recently reported by Abdo et al. (2011c). Figure 13 overlays H.E.S.S. TeV contours of SNR RX J1713.7−3946 from Aharonian et al. (2007b). To analyze this source, we used the same background source model as the recent LAT publication.

8.4. 2FGL J0851.7−4635

2FGL J0851.7−4635 was found to have an extension of $1°13 \pm 0°08_{\text{stat}} \pm 0°05_{\text{sys}}$ with an extension significance of $\text{TS}_{\text{ext}} = 87.2$ using photons with energies between 10 GeV and 100 GeV. This source was fit to $(l, b) = (266°29, -1°43)$ and figure 14 shows a counts map of the source. 2FGL J0851.7−4635 is spatially coincident with the SNR Vela Jr. Overlaid on Figure 14 are H.E.S.S. TeV contours of Vela Jr. (Aharonian et al. 2007a). The GeV and TeV morphology match well. A detailed papers by the LAT Collaboration on Vela Jr. is in preparation.

To get a good fit of this source, we had to remove from our background model 2FGL J0853.5−4711, 2FGL J0848.5−4535, and 2FGL J0855.4−4625 which were included in 2FGL to account for part of the extended emission. In addition, we relocalized 2FGL J0854.7−4501 to $(l, b) =$

(266°.24, 0°.49) to better fit its position at high energies and we had to remove from our model 2FGL J0858.0−4815 and 2FGL J0901.7−4655 because they were not significant above 10 GeV.

8.5.   2FGL J1615.0−5051

2FGL J1615.0−5051 was found to have an extension of $0°.33\pm0°.04_{\rm stat}\pm0°.01_{\rm sys}$ with an extension significance of $\rm TS_{ext}$ =16.3 using photons with energies between 10 GeV and 100 GeV. This source was fit to $(l, b) = (332°.38, −0°.14)$ and is coincident with 1FGL J1613.6−5100c. Figure 15 shows a counts map of the source. It is less than $1°$ away from 2FGL J1615.2−5138 which is also spatially extended (see Section 8.6). To get a good fit of both sources, we modeled both of them as being spatially extended and iteratively fit the position and extension of each source. We had to remove from our background model 2FGL J1614.9−5212 which was included in 2FGL to account for part of the extended emission. We also removed from our model 2FGL J1619.7−5040c and 2FGL J1620.6−5111c because they were not significant above 10 GeV.

2FGL J1615.2−5138 is spatially coincident with the extended and TeV contours are overlaid on Figure 15 (Aharonian et al. 2006). H.E.S.S. measured an extension $0°.136\pm0°.008$ when fitting this source with an elliptical 2D Gaussian surface brightness. This corresponds to a 68% containment radius of $\rm r_{68} = 0°.21 \pm 0°.01$, comparable to the LAT size $\rm r_{68} = 0°.27\pm0°.03$. Figure 19 shows that the spectrum of 2FGL J1615.0−5051 at GeV energies also connects smoothly to the spectrum of HESS J1616−508 at TeV energies.

HESS J1616−508 is located in the region of two SNRs RCW103 (G332.4-04) and Kes 32 (G332.4+0.1) but is not spatially coincident with either of them (Aharonian et al. 2006). HESS J1616−508 is near three pulsars PSR J1614−5048, PSR J1616−5109, and PSR J1617−5055. (Torii et al. 1998; Landi et al. 2007a). Only PSR J1617−5055 is energetically capable of powering the TeV emission and Aharonian et al. (2006) speculated that HESS J1616−508 could be a PWN powered by this young pulsar. Because HESS J1616−508 is $9'$ away from PSR J1617−5055, this would require an asymmetric X-ray PWNe to power the TeV emission. *Chandra* ACIS observations revealed an underluminous PWN of size $\sim 1'$ around the pulsar that was not oriented towards the TeV emission rendering this association uncertain (Kargaltsev et al. 2009). No other promising counterparts were observed at X-ray and soft gamma-ray energies by *Suzaku* (Matsumoto et al. 2007), *Swift*/XRT, IBIS/ISGRBI, BeppoSAX and *XMM-Newton* (Landi et al. 2007a). Kargaltsev et al. (2009) discovered some additional diffuse emission towards the center of HESS J1616−508 using archival radio and infared observations. Deeper observations will likely be necessary to understand this γ-ray

source.

8.6. 2FGL J1615.2−5138

2FGL J1615.2−5138 was found to have an extension of $0°.42 \pm 0°.03_{stat} \pm 0.01_{sys}$ with an extension significance of $TS_{ext} = 48.0$ using photons with energies between 10 GeV and 100 GeV. This source was fit to $(l, b) = (331°.66, -0°.66)$ and is coincident with 1FGL J1614.7−5138c. Because 2FGL J1615.2−5138 is close to 2FGL J1615.0−5051, the same model described in Section 8.5 was used to analyze both sources. Both sources can be seen in Figure 15.

This source is spatially coincident with the extended TeV source HESS J1614−518 and TeV contours are ovlaid on Figure 15 (Aharonian et al. 2006). H.E.S.S. measured a 2D Gaussian extension of $\sigma = 0°.23 \pm 0°.02$ and $\sigma = 0°.15 \pm 0°.02$ in the semi-major and semi-minor axis. This corresponds to a 68% containment size of $r_{68} = 0°.35 \pm 0°.03$ and $0°.23 \pm 0°.03$, consistent with the LAT size $r_{68} = 0°.35 \pm 0°.03$. Figure 19 shows that the spectrum of 2FGL J1615.2−5138 at GeV energies connects smoothly to the spectrum of HESS J1614−518 at TeV energies. Further data collected by H.E.S.S. in 2007 resolve a double peaked structure at TeV energies but no spectral variation across this source, suggesting that the emission is not the confusion of physically separate sources (Rowell et al. 2008). The source was also detected by CANGAROO-III (Mizukami et al. 2011).

There are five nearby pulsars, but none are luminous enough to provide the energy output required to power the TeV emission (Rowell et al. 2008). HESS J1614−518 is spatially coincident with a young open cluster Pismis 22 (Landi et al. 2007b; Rowell et al. 2008). *Suzaku* detected two promising X-ray candidates. Source A is an extended source consistent with the peak of HESS J1614−518 and source B coincident with Pismis 22 and towards the center but in a relatively dim region of HESS J1614−518 (Matsumoto et al. 2008). Three hypothesis have been presented to explain this emission; either source A is an SNR powering the γ-ray emission, source A is a PWN powered by an undiscovered pulsar in either source A or B, and finally that the emission may arise from hadronic acceleration in the stellar winds of Pisim 22 (Mizukami et al. 2011).

8.7. 2FGL J1632.4−4753c

2FGL J1632.4−4753c was found to have an extension of $0°.44 \pm 0°.04_{stat} \pm 0°.03_{sys}$ with an extension significance of $TS_{ext} = 64.5$ using photons with energies between 10 GeV and 100 GeV. This source was fit to $(l, b) = (336°.41, 0°.22)$ and is coincident with 1FGL J1632.9−4802c.

Figure 16 shows a counts map of this source. To get a good fit of this source, we had to remove from our background model three sources 2FGL J1631.7−4720c, 2FGL J1630.2−4752, 2FGL J1634.4−4743c.4-4820c which were included in 2FGL to account for part of the extended emission. We relocalized 2FGL J1635.4−4717c to $(l, b) = (337°23, 0°35)$ and 2FGL J1636.3−4740c to $(l, b) = (336°97, −0°07)$ and removed from our model four farther away sources 2FGL J1638.0−4703c, 2FGL J1628.1−4857c, 2FGL J1630.1−4615, 2FGL J1639.8−4921c because they were not significant above 10 GeV.

This extended source is spatially coincident with the extended TeV source HESS J1632−478 and TeV contours are overlaid on Figure 16 (Aharonian et al. 2006). H.E.S.S measured a extension of $\sigma = 0°21 \pm 0°05$ and $0°06 \pm 0°04$ along the semi-major and semi-minor axes when fitting this source with an elliptical 2D Gaussian surface brightness. This corresponds to a 68% containment size $r_{68} = 0°31 \pm 0°08$ and $0°09 \pm 0°06$ along the semi-major and semi-minor axis, consistent with the LAT size $r_{68} = 0°36 \pm 0°04$. Figure 19 shows that the spectrum of 2FGL J1635.4−4717c at GeV energies connects smoothly to the spectrum of HESS J1632−478 at TeV energies.

Aharonian et al. (2006) argued that HESS J1632−478 is positionally coincident with the hard X-ray source IGR J1632-4751 observed by *ASCA*, INTEGRAL, and *XMM-Newton* (Sugizaki et al. 2001; Tomsick et al. 2003; Rodriguez et al. 2003), but this source is suspected to be a galactic X-Ray Binary so the γ-ray extension disfavors the association. Further observations by *XMM-Newton* discovered point-like emission coincident with the peak of the H.E.S.S. source surrounded by extended emission of size $\sim 32'' \times 15''$ (Balbo et al. 2010). They found in archival MGPS-2 data a spatially coincident extended radio source (Murphy et al. 2007) and argued for a single synchrotron process producing the radio, X-ray, and TeV emission, likely due to a PWNe. The increased size at TeV energies compared to X-ray energies has previously been observed in several aging PWNe including HESS J1825−137 (Gaensler et al. 2003; Aharonian et al. 2006b), HESS J1640−465 (Aharonian et al. 2006; Funk et al. 2007), and Vela X (Markwardt & Ogelman 1995; Aharonian et al. 2006c) and can be explained by different synchrotron cooling times for the electrons that produce X-rays and γ-rays.

8.8.   2FGL J1837.3−0700c

2FGL J1837.3−0700c was found to have an extension of $0°35 \pm 0°08_{\mathrm{stat}} \pm 0°03_{\mathrm{sys}}$ with an extension significance of $\mathrm{TS_{ext}} = 18.8$ using photons with energies between 10 GeV and 100 GeV. This source was fit to $(l, b) = (25°08, 0°13)$ and is coincident with 1FGL J1837.5−0659c. Figure 17 shows a counts map of this source. It is in a complicated region with three nearby

sources 2FGL J1834.7−0705c, 2FGL J1836.8−0623c, and 2FGL J1839.3−0558c. To get a good fit of 2FGL J1837.3−0700c, we relocalized 2FGL J1834.7−0705c to $(l, b) = (24°77, 0°50)$, 2FGL J1836.8−0623c to $(l, b) = (25°57, 0°32)$, and 2FGL J1839.3−0558c to $(l, b) = (26°08, 0°23)$. We had to remove from our background model 2FGL J1835.5−0649 which was included in 2FGL to account for part of the extended emission and also 2FGL J1839.0−0539 because it was not significant above 10 GeV.

This source is spatially coincident with the TeV source HESS J1837−069 and TeV contours are overlaid on Figure 17 (Aharonian et al. 2006). H.E.S.S. measured an extension of $\sigma = 0°12 \pm 0°02$ and $0°05 \pm 0°02$ along the semi-major and semi-minor axis when fitting this source with an elliptical 2D Gaussian surface brightness. This corresponds to a 68% containment radius of $r_{68} = 0°18 \pm 0°03$ and $0°08 \pm 0°03$ along the semi-major and semi-minor axis. The size is not significantly different from the LAT 68% containment radius of $r_{68} = 0°29 \pm 0°07$ (less than 2σ). Figure 19 shows that the spectrum of 2FGL J1837.3−0700c at GeV energies connects smoothly to the spectrum of HESS J1837−069 at TeV energies.

HESS J1837−069 is coincident with the hard and steady X-ray source AX J1838.0−0655 (Hertz & Grindlay 1988; Bamba et al. 2003; Malizia et al. 2005; Landi et al. 2006; Gotthelf & Halpern 2008; Anada et al. 2009). This source was discovered by RXTE to be a pulsar sufficiently luminous to power the TeV emission. AX J1838.0−0655 was spatially resolved by *Chandra* to be a bright point-like source surrounded by a $\sim 2'$ nebula (Gotthelf & Halpern 2008). The γ-ray emission may be powered by this pulsar. A second X-ray point-like source AX J1837.3−0652 is near HESS J1837−069 (Bamba et al. 2003; Landi et al. 2006; Gotthelf & Halpern 2008; Anada et al. 2009). It was also resolved into point-like and diffuse component although no pulsations have been detected from it (Gotthelf & Halpern 2008). Some of the γ-ray emission could also come from AX J1837.3−0652.

8.9.   2FGL J2021.5+4026

2FGL J2021.5+4026 was found to have an extension of $0°59 \pm 0°03_{\mathrm{stat}} \pm 0°02_{\mathrm{sys}}$ with an extension significance of $\mathrm{TS_{ext}} = 116.4$ using photons with energies between 10 GeV and 100 GeV. This source was fit to $(l, b) = (78°18, 2°19)$ and is coincident with 1FGL J2020.0+4049. Figure 18 shows a counts map of this source and Figure 11 shows its spectrum. To get a good fit of this source, we had to remove from our background model 2FGL J2019.1+4040 which was included in 2FGL to account for part of the extended emission. Further, it was necessary to add to our region an additional point-like source at $(l, b) = (78°85, 2°67)$. Although this source is not very significant (TS = 13.5), not including it in the background model significantly biased the fit extension. In addition, we had to remove from our model the four sources

2FGL J2022.8+3843c, 2FGL J2020.0+4159, 2FGL J2013.8+4115c, and 2FGL J2012.4+3955c because they were not significant above 10 GeV.

This extended sources is coincident with 2CG 078+01 and 3EG J2020+4017 (Swanenburg et al. 1981; Hartman et al. 1999) and also with the γ-Cygni SNR. This γ-ray source has been speculated to originate from the interaction of accelerated particles in the SNR interacting with dense molecular clouds (Pollock 1985; Gaisser et al. 1998), but this association was disfavored when the LAT GeV emission from this source was detected to be pulsed (PSR J2021+4026, Abdo et al. (2010m)).

Milagro detected a 4.2σ excess at energies ~ 30 TeV from this location (Abdo et al. 2009c,d). Veritas also detected an extended source VER J2019+407 coincident with the SNR above 200 GeV and suggested that the TeV emission could be a shock-cloud interaction in γ-Cygni (Weinstein 2009). Using just photons with energies between 10 GeV to 100 GeV where PSR J2021+4026 is not significant, we resolved an extended source whose inferred size at GeV energies well matches the radio size of γ-Cygni. This can be seen clearly in Figure 18 which overlays radio contours of γ-Cygni from the Canadian Galactic Plane Survey (Taylor et al. 2003).

9. Discussion

Twelve extended sources were included in 2FGL. Using two years of LAT data and a new analysis method, we presented the detection of nine additional extended sources. We also reanalyze the spatial shape of the twelve extended sources in 2FGL. The 21 extended LAT sources are primarily along the Galactic plane and their locations are shown in Figure 20. Most of the LAT detected extended sources are expected to be of Galactic origin as the distance of extragalactic sources (with the exception of the local group Galaxies) is typically too large to be able to resolve them at γ-rays energies.

For the LAT extended sources also seen at TeV energies, Figure 21 shows that there is a good correlation between the size of the sources at GeV and TeV energies. Even so, the size of PWNe are expected to vary across the GeV and TeV energy range and the size of HESS J1825−137 is significantly larger at GeV than TeV energies (Grondin et al. 2011). It is interesting to compare the size of other PWN candidates at GeV and TeV energies, but definitively measuring this would require a more in-depth analysis of the LAT data using the same elliptical surface brightness model.

Figure 22 compares the size of the 21 extended LAT sources to the 42 extended H.E.S.S.

sources.[7] Because of the large field of view and all-sky coverage, the LAT can more easily measure larger sources. On the other hand, the better angular resolution of air Cherenkov detectors allows them to measure a population of extended sources below our detection threshold limit (currently about $\sim 0°\!.2$). *Fermi* has a five year nominal mission lifetime with a goal of ten years of operation. As Figure 6 shows, the LAT's low background at high energies allows its sensitivity to these smaller sources to improve by a factor greater than the square root of the exposure. With increasing exposure, the LAT will likely begin to detect and resolve some of these smaller TeV sources.

Figure 23 compares the spectral index of LAT detected extended sources and of all sources in 2FGL. This, and Table 3 and 4, show that the LAT observes a population of hard extended sources at energies above 10 GeV. Figure 19 shows that the spectra of four of these sources (2FGL J1615.0−5051, 2FGL J1615.2−5138, 2FGL J1632.4−4753c, and 2FGL J1837.3−0700c) at GeV energies connects smoothly to the spectra of their H.E.S.S. counterparts at TeV energies. This is also true of Vela Jr., HESS J1825−137 (Grondin et al. 2011), and RX J1713.7−3946 (Abdo et al. 2011c). It is likely that the GeV and TeV emission from these sources originates from the same population of high-energy particles.

Many of the TeV detected extended sources now seen at GeV energies are currently unidentified and further multi-wavelength follow-up observations will be necessary to understand these particle accelerators. But the extension of the spectrum of these TeV sources towards lower energies by LAT observations can help to determine the origin and nature of the high-energy emission seen from these sources.

REFERENCES

Abdo, A. A., et al. 2009a, Physical Review Letters, 103, 251101

—. 2009b, ApJ, 706, L1

—. 2009c, ApJS, 183, 46

—. 2009d, ApJ, 700, L127

—. 2009e, Astroparticle Physics, 32, 193

—. 2010a, ApJ, 714, 927

---

[7]The TeV extension of the 42 extended H.E.S.S. sources comes from the H.E.S.S. Source Catalog. The H.E.S.S. source catalog can be found at `http://www.mpi-hd.mpg.de/hfm/HESS/pages/home/sources/`.

—. 2010b, A&A, 523, A46+

—. 2010c, Science, 328, 725

—. 2010d, ApJS, 188, 405

—. 2010e, ApJ, 718, 348

—. 2010f, ArXiv e-prints

—. 2010g, ArXiv e-prints

—. 2010h, Science, 327, 1103

—. 2010i, ApJ, 712, 459

—. 2010j, A&A

—. 2010k, Physical Review Letters, 104, 101101

—. 2010l, ApJ, 715, 429

—. 2010m, ApJS, 187, 460

—. 2011a, Astroparticle Physics, in preparation

—. 2011b, ArXiv e-prints

—. 2011c, ApJ, 734, 28

Acciari, V. A., et al. 2009, ApJ, 698, L133

—. 2011, ArXiv e-prints

Ackermann, M., et al. 2011, ArXiv e-prints

Aharonian, F., et al. 2005, A&A, 435, L17

—. 2006a, A&A, 460, 743

—. 2006b, A&A, 460, 365

—. 2006c, A&A, 448, L43

Aharonian, F., et al. 2006, ApJ, 636, 777

Aharonian, F., et al. 2007a, ApJ, 661, 236

—. 2007b, A&A, 464, 235

—. 2008, A&A, 481, 401

Aharonian, F. A., Coppi, P. S., & Voelk, H. J. 1994, ApJ, 423, L5

Aharonian, F. A., et al. 2007c, A&A, 469, L1

Albert, J., et al. 2006, Science, 312, 1771

Anada, T., Ebisawa, K., Dotani, T., & Bamba, A. 2009, PASJ, 61, 183

Atwood, W. B., et al. 2009, ApJ, 697, 1071

Balbo, M., Saouter, P., Walter, R., Pavan, L., Tramacere, A., Pohl, M., & Zurita-Heras, J.-A. 2010, A&A, 520, A111+

Baltz, E. A., et al. 2008, J. Cosmology Astropart. Phys., 7, 13

Bamba, A., Ueno, M., Koyama, K., & Yamauchi, S. 2003, ApJ, 589, 253

Blandford, R., & Eichler, D. 1987, Phys. Rep., 154, 1

Castelletti, G., Dubner, G., Golap, K., & Goss, W. M. 2006, A&A, 459, 535

Castro, D., & Slane, P. 2010, ApJ, 717, 372

Dame, T. M. 2011, ArXiv e-prints

de Geus, E. J., Bronfman, L., & Thaddeus, P. 1990, A&A, 231, 137

Eadie, W. T., Drijard, D., & James, F. E. 1971, Statistical methods in experimental physics, ed. Eadie, W. T., Drijard, D., & James, F. E.

Funk, S., Hinton, J. A., Pühlhofer, G., Aharonian, F. A., Hofmann, W., Reimer, O., & Wagner, S. 2007, ApJ, 662, 517

Gaensler, B. M., Schulz, N. S., Kaspi, V. M., Pivovaroff, M. J., & Becker, W. E. 2003, ApJ, 588, 441

Gaisser, T. K., Protheroe, R. J., & Stanev, T. 1998, ApJ, 492, 219

Górski, K. M., Hivon, E., Banday, A. J., Wandelt, B. D., Hansen, F. K., Reinecke, M., & Bartelmann, M. 2005, ApJ, 622, 759

Gotthelf, E. V., & Halpern, J. P. 2008, ApJ, 681, 515

738 Grenier, I. A., Casandjian, J.-M., & Terrier, R. 2005, Science, 307, 1292

739 Grondin, M. ., et al. 2011, ArXiv e-prints

740 Hartman, R. C., et al. 1999, ApJS, 123, 79

741 Hertz, P., & Grindlay, J. E. 1988, AJ, 96, 233

742 Hwang, U., Petre, R., & Flanagan, K. A. 2008, ApJ, 676, 378

743 James, F., & Roos, M. 1975, Comput. Phys. Commun., 10, 343

744 Kargaltsev, O., Pavlov, G. G., & Wong, J. A. 2009, The Astrophysical Journal, 690, 891

745 Katagiri, H., et al. 2011, ArXiv e-prints

746 Kerr, M. 2011, PhD in physics, University of Washington

747 King, I. 1962, AJ, 67, 471

748 Krause, J., Carmona, E., & Reichardt, I. 2011, in (Presented at the 2011 Fermi Symposium,
749   Rome Italy)

750 Landi, R., de Rosa, A., Dean, A. J., Bassani, L., Ubertini, P., & Bird, A. J. 2007a, MNRAS,
751   380, 926

752 Landi, R., Masetti, N., Bassani, L., Cellone, S. A., Romero, G. E., Ubertini, P., & Dean,
753   A. J. 2007b, The Astronomer's Telegram, 1047, 1

754 Landi, R., et al. 2006, ApJ, 651, 190

755 Malizia, A., et al. 2005, ApJ, 630, L157

756 Markwardt, C. B., & Ogelman, H. 1995, Nature, 375, 40

757 Matsumoto, H., et al. 2007, PASJ, 59, 199

758 —. 2008, PASJ, 60, 163

759 Mattox, J. R., et al. 1996, ApJ, 461, 396

760 Mizukami, T., et al. 2011, ArXiv e-prints

761 Murphy, T., Mauch, T., Green, A., Hunstead, R. W., Piestrzynska, B., Kels, A. P., &
762   Sztajer, P. 2007, MNRAS, 382, 382

Paron, S., Dubner, G., Reynoso, E., & Rubio, M. 2008, A&A, 480, 439

Petre, R., Becker, C. M., & Winkler, P. F. 1996, ApJ, 465, L43+

Pollock, A. M. T. 1985, A&A, 150, 339

Protassov, R., van Dyk, D. A., Connors, A., Kashyap, V. L., & Siemiginowska, A. 2002, ApJ, 571, 545

Reynoso, E. M., Dubner, G. M., Goss, W. M., & Arnal, E. M. 1995, AJ, 110, 318

Reynoso, E. M., Green, A. J., Johnston, S., Dubner, G. M., Giacani, E. B., & Goss, W. M. 2003, MNRAS, 345, 671

Rodriguez, J., Tomsick, J. A., Foschini, L., Walter, R., Goldwurm, A., Corbel, S., & Kaaret, P. 2003, A&A, 407, L41

Rowell, G., Horns, D., Fukui, Y., & Moriguchi, Y. 2008, in American Institute of Physics Conference Series, Vol. 1085, American Institute of Physics Conference Series, ed. F. A. Aharonian, W. Hofmann, & F. Rieger, 241–244

Sreekumar, P., et al. 1998, The Astrophysical Journal, 494, 523

Sugizaki, M., Mitsuda, K., Kaneda, H., Matsuzaki, K., Yamauchi, S., & Koyama, K. 2001, ApJS, 134, 77

Swanenburg, B. N., et al. 1981, ApJ, 243, L69

Taylor, A. R., et al. 2003, AJ, 125, 3145

Tomsick, J. A., Lingenfelter, R., Walter, R., Rodriguez, J., Goldwurm, A., Corbel, S., & Kaaret, P. 2003, IAU Circ., 8076, 1

Torii, K., et al. 1998, ApJ, 494, L207+

Weekes, T. C., et al. 1989, ApJ, 342, 379

Weinstein, A. 2009, ArXiv e-prints

Young, E. T., Lada, C. J., & Wilking, B. A. 1986, ApJ, 304, L45

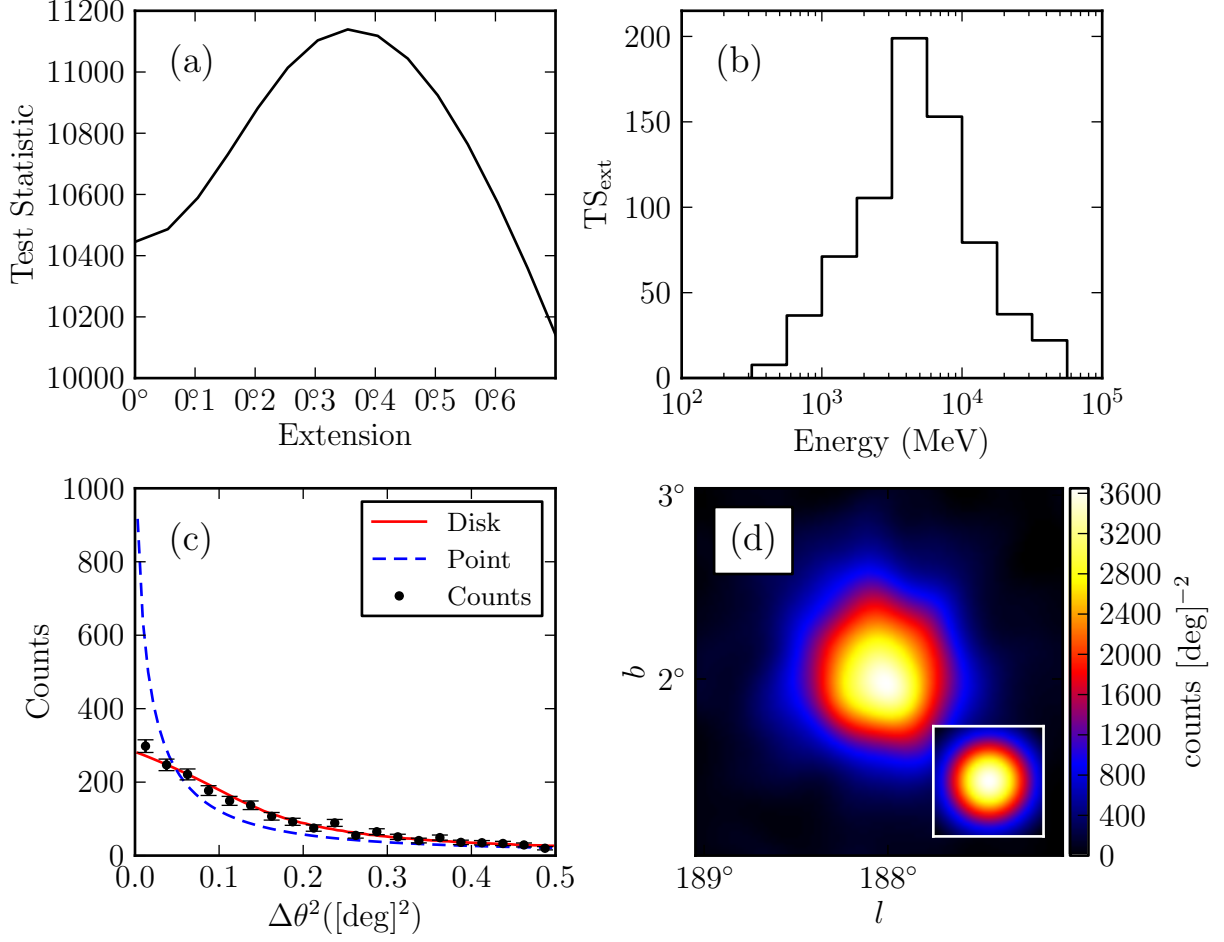Fig. 1.— Counts maps and test statistic profiles for the SNR IC443. (a) TS vs. extension of the source. (b) $\mathrm{TS_{ext}}$ for individual energy bands. (c) observed radial profile of counts in comparison to the expected profiles for a spatially extended source (solid and colored red in the online version) and for a point-like source (dashed and colored blue in the online version). (d) smoothed count map after subtraction of the diffuse emission compared to the smoothed LAT PSF (inset). Plots (a), (c), and (d) use only photons with energies between 1 GeV and 100 GeV. Plots (c) and (d) use only photons which converted in the front part of the tracker and have an improved angular resolution.
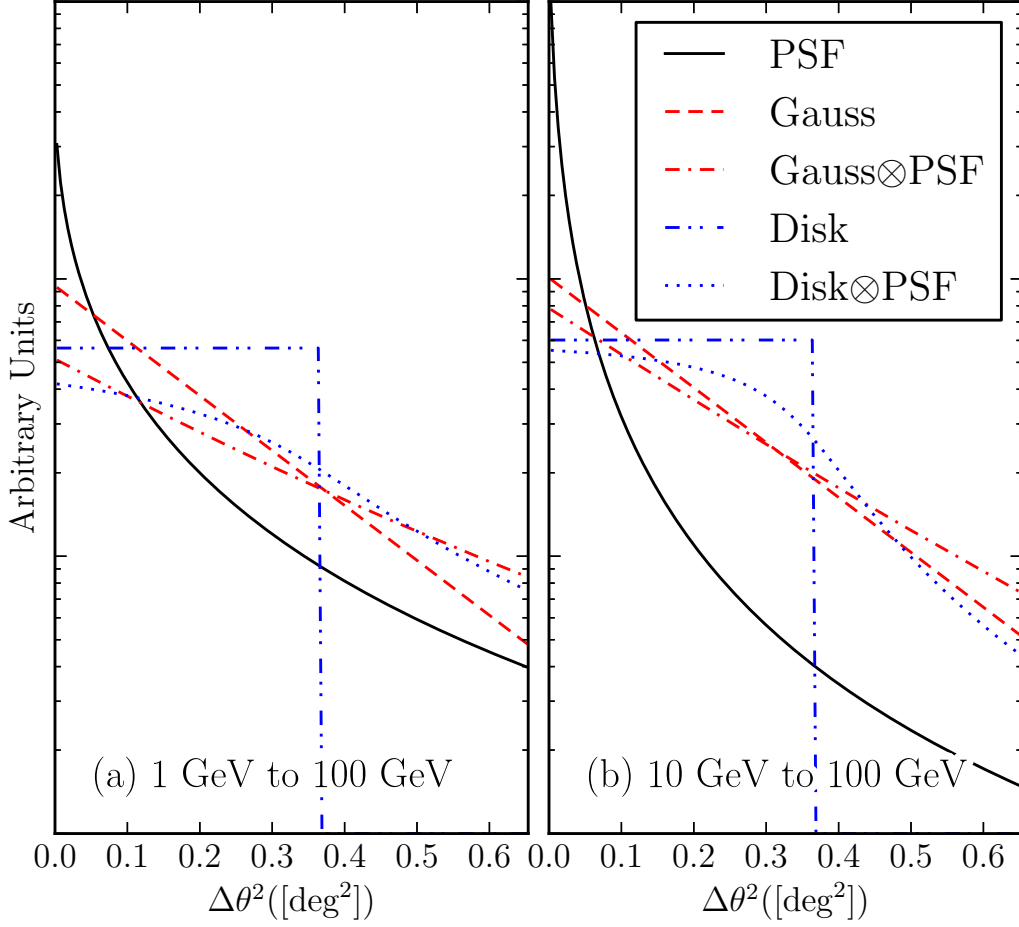
Fig. 2.— A comparison of a 2D Gaussian and uniform surface brightness profiles of extended sources before and after convolving with the PSF for two energy ranges. The solid black line is the PSF that would be observed for a power-law source of spectral index 2. The dashed line and the dash-dotted lines are the brightness profile of a Gaussian with $r_{68} = 0°.5$ and the convolution of this profile with the LAT PSF respectively (colored red in the online version). The dash-dot-doted and the dot-doted lines are the brightness profile of a uniform disk with $r_{68} = 0°.5$ and the convolution of this profile with the LAT PSF respectively (colored blue in the online version).

Table 1.   Monte Carlo Spectral Parameters

Spectral Index	Flux[a] (ph cm^{-2} s^{-1})	N_{sims}	$\langle \mathrm{TS} \rangle$
1.5	10^{-6}	31952	92862
	3×10^{-7}	31962	22169
	10^{-7}	31977	5806
	3×10^{-8}	31991	1270
	10^{-8}	31940	301
	3×10^{-9}	30324	62
2	10^{-6}	31872	22067
	3×10^{-7}	31890	4898
	10^{-7}	31858	1097
	3×10^{-8}	31632	236
	10^{-8}	27491	103
2.5	10^{-6}	31822	4706
	3×10^{-7}	31822	889
	10^{-7}	31169	176
	3×10^{-8}	21591	41
3	10^{-6}	31763	929
	3×10^{-7}	31665	161
	10^{-7}	19271	40

[a]Integral 1 GeV to 100 GeV flux.

Note. — A list of the spectral models of the simulated point-like sources which were tested for extension. For each model, the number of statistically independent simulations and the average value of TS is also tabulated. The models span representative spectral parameters.
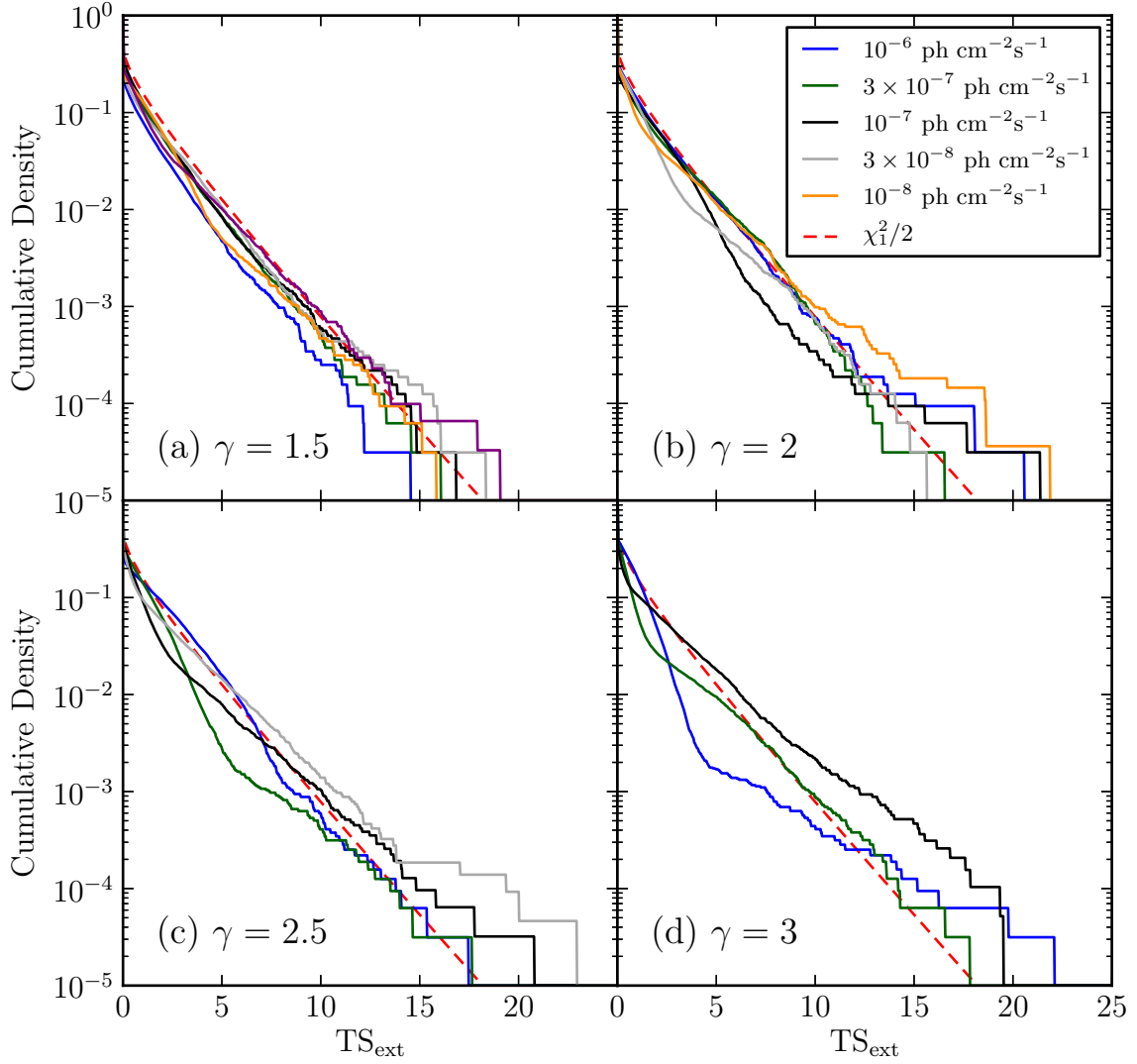
Fig. 3.— Distribution of the test statistic for the extension test. The four plots represent simulated point-like sources of different spectral indices and the different lines (colored in the online version) represent point-like sources with different 100 MeV to 100 GeV integral fluxes. The dashed line (colored red) is the cumulative density function of Equation 9.

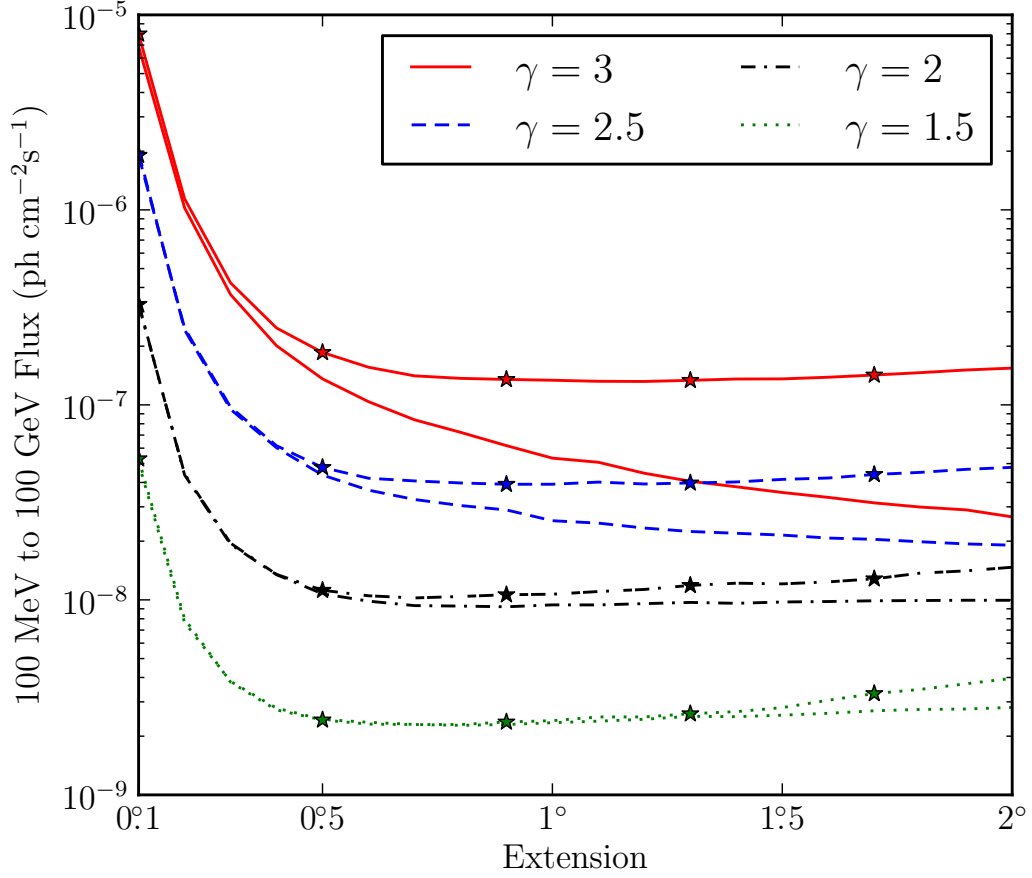Fig. 4.— The detection threshold to resolve a uniform surface brightness extended source for a two-year exposure. All sources have an assumed power-law spectrum and the different colors correspond to different simulated spectral indices. The solid line is the detection threshold using photons with energies between 100 MeV and 100 GeV while the dashed line is the threshold using photons with energies between 1 GeV and 100 GeV.
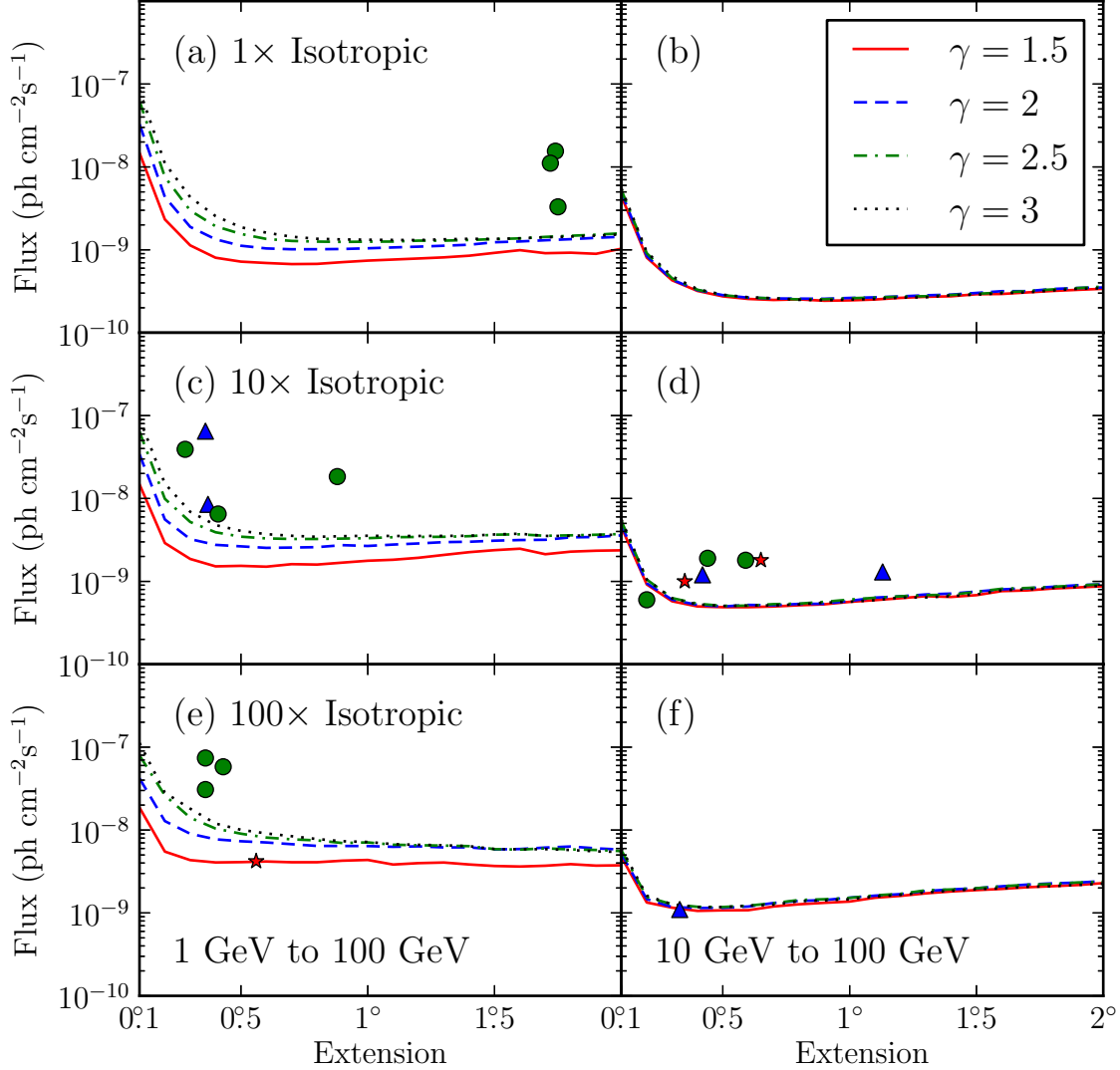
Fig. 5.— the LAT detection threshold for four spectral indices and three background (1×, 10×, and 100× the Sreekumar-like isotropic background) for a two-year exposure. The left plots are the detection threshold when using photons with energies between 1 GeV and 100 GeV and the right plots are the detection threshold when using photons with energies between 10 GeV and 100 GeV. The flux is integrated only in the selected energy range. Overlaid on this plot are the LAT detected extended sources placed by the magnitude of the nearby Galactic diffuse emission and the energy range they were analyzed with. The star-shaped markers (colored red in the electronic version) are sources with a spectral index closer to 1.5, the triangular markers (colored blue) an index closer to 2, and the circular markers (colored green) an index closer to 2.5. The circular marker in plot (d) below the sensitivity line is MSH 15−52.

Table 2.   Extension Detection Threshold

γ	BG	0.1	0.2	0.3	0.4	0.5	0.6	0.7	0.8	0.9	1.0	1.1	1.2	1.3	1.4	1.5	1.6	1.7	1.8	1.9	2.0
									E>1 GeV												
1.5	1×	148.1	23.3	11.3	8.0	7.2	6.9	6.7	6.8	7.1	7.4	7.6	7.9	8.1	8.5	9.2	9.9	9.1	9.2	9.0	10.3
	10×	148.4	29.0	18.7	15.2	15.4	15.0	16.1	16.0	16.8	17.7	18.2	19.3	20.9	22.5	23.8	24.8	21.3	22.8	23.4	23.7
	100×	186.8	55.0	43.4	40.7	41.0	41.8	40.9	40.9	42.7	43.6	38.4	39.9	40.6	38.4	36.9	36.3	37.1	38.8	37.2	37.6
2	1×	328.4	43.4	18.9	13.4	11.2	10.4	10.2	10.2	10.2	10.4	10.7	10.9	11.2	11.5	12.4	12.6	13.0	13.4	14.0	14.4
	10×	341.0	55.9	32.3	27.6	26.5	25.4	25.6	25.9	27.4	26.8	27.8	28.7	29.8	30.1	31.0	31.5	31.7	34.0	34.3	35.9
	100×	420.5	128.3	90.2	77.3	73.3	70.8	67.5	64.3	64.2	64.1	62.8	63.6	61.7	61.9	58.4	59.0	61.4	63.3	60.1	58.1
2.5	1×	627.1	75.6	29.8	19.3	15.5	13.5	12.8	12.6	12.5	12.5	12.6	12.9	12.9	13.1	13.5	13.7	14.3	14.8	15.2	15.8
	10×	638.9	99.1	52.1	39.1	34.6	33.0	32.5	32.5	32.8	33.2	34.1	34.3	34.5	35.1	36.6	36.9	35.5	36.0	36.5	37.3
	100×	795.0	262.1	140.9	104.3	90.4	81.2	77.2	75.1	69.7	70.9	66.5	65.6	64.9	64.0	58.9	58.1	60.2	58.4	57.5	55.8
3	1×	841.5	110.6	43.2	25.5	18.7	16.1	14.4	13.6	13.3	13.2	13.1	13.1	13.4	13.6	13.5	13.8	14.2	14.4	14.8	15.4
	10×	921.6	151.3	69.1	47.8	40.7	37.1	35.5	34.5	35.1	35.5	35.3	35.3	35.4	35.5	36.8	37.6	35.3	35.4	36.3	36.6
	100×	1124.1	282.9	181.1	119.8	100.7	91.1	84.3	77.9	73.3	71.8	67.6	66.4	65.5	63.9	59.0	58.6	58.8	57.5	55.4	54.4
									E>10 GeV												
1.5	1×	44.6	8.0	4.3	3.2	2.7	2.6	2.5	2.5	2.4	2.5	2.5	2.6	2.7	2.8	2.9	2.9	3.1	3.2	3.3	3.4
	10×	45.2	9.2	5.8	5.0	4.9	4.9	5.0	5.2	5.3	5.7	5.9	6.3	6.6	6.5	6.8	7.6	7.8	8.2	8.5	8.7
	100×	47.3	13.4	11.6	10.6	10.8	10.8	12.0	12.7	13.2	13.7	15.3	16.1	17.2	18.2	18.9	19.5	20.4	21.0	21.7	22.9
2	1×	49.7	8.4	4.4	3.3	2.8	2.6	2.6	2.6	2.6	2.6	2.7	2.7	2.8	2.9	3.0	3.2	3.2	3.4	3.5	3.5
	10×	48.6	9.5	6.0	5.2	5.0	5.2	5.2	5.3	5.4	5.8	6.4	6.6	7.0	7.1	7.5	8.0	8.3	8.6	9.0	9.2
	100×	51.8	14.7	11.8	11.5	11.5	11.9	13.2	14.0	14.3	15.3	16.2	16.9	18.4	19.2	19.8	21.0	22.0	22.8	23.2	24.3
2.5	1×	53.1	9.1	4.5	3.3	2.8	2.7	2.6	2.5	2.5	2.6	2.7	2.7	2.8	2.8	2.9	3.1	3.2	3.3	3.5	3.6
	10×	53.7	10.5	6.3	5.4	5.1	5.1	5.3	5.4	5.7	6.0	6.3	6.6	6.8	6.9	7.5	8.1	8.3	8.6	8.9	9.2
	100×	57.0	15.6	12.7	11.9	11.8	12.2	13.1	14.3	14.6	15.2	16.3	17.0	18.8	19.2	19.9	21.0	21.9	22.3	23.3	23.7
3	1×	55.5	9.4	4.8	3.4	2.9	2.7	2.6	2.5	2.5	2.5	2.6	2.7	2.7	2.8	2.9	3.0	3.1	3.2	3.4	3.4
	10×	56.0	10.5	6.2	5.3	5.1	5.1	5.1	5.3	5.5	5.7	5.9	6.4	6.4	6.6	7.0	7.8	8.0	8.3	8.6	8.9
	100×	60.3	16.2	12.7	11.7	11.8	12.2	12.6	13.8	14.2	14.6	15.8	16.5	17.6	18.5	19.4	19.8	20.7	21.0	21.8	22.5

Note. — The detection threshold to resolve spatially extended sources with a uniform surface brightness for a two-year exposure The threshold is calculated for sources of varying energy ranges, spectral indices, and background levels. The sensitivity was calculated against a Sreekumar-like isotropic background and the second column is the factor that the simulated background was scaled by. The remaining columns are varying sizes of the source. The table quotes integral fluxes in the analyzed energy range (1 GeV to 100 GeV or 10 GeV 100 GeV) in units of 10^{-10} ph cm^{-2} s^{-1}.
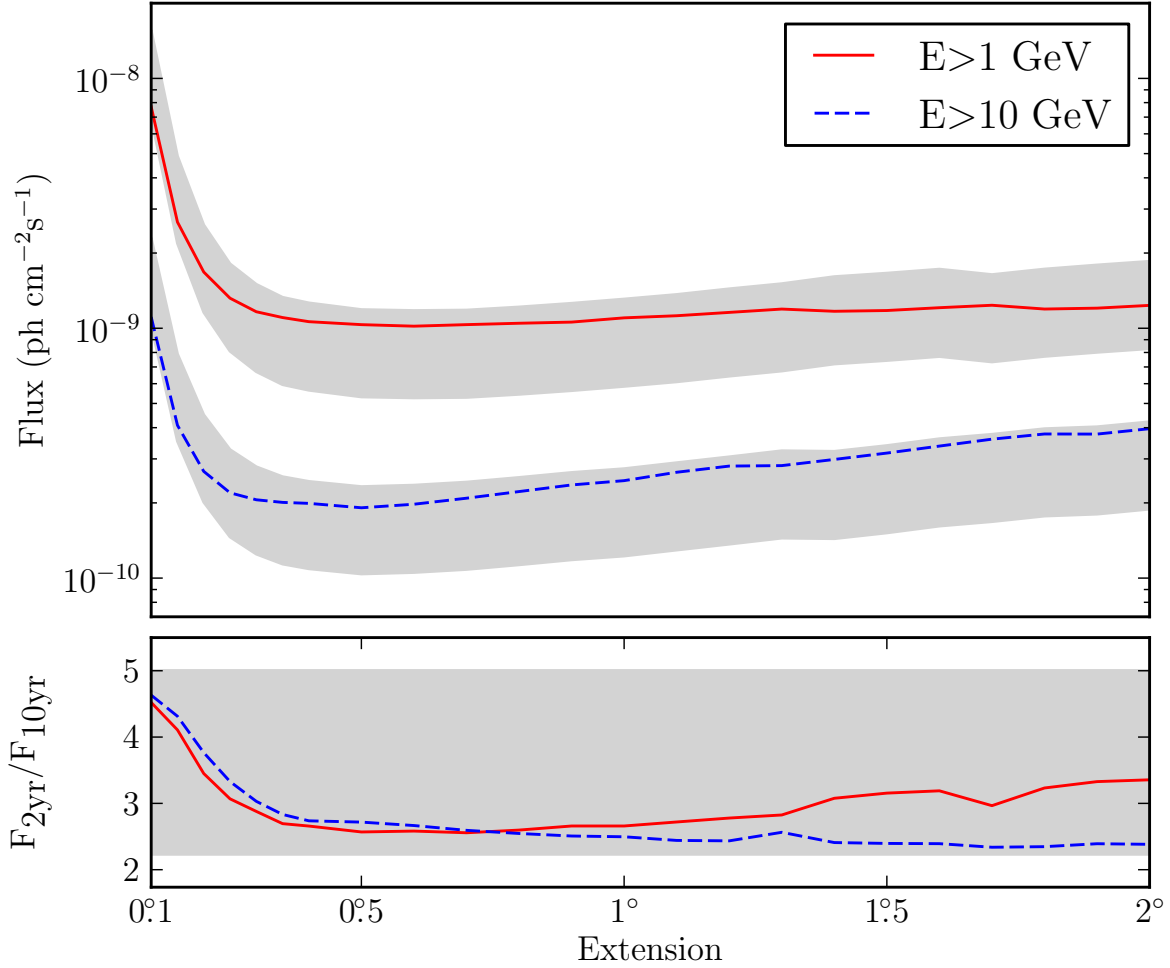
Fig. 6.— The LAT's projected detection threshold to extension after a ten-year exposure for a power-law source of spectral index 2 against 10 times the isotropic background in the energy range from 1 GeV to 100 GeV (solid line colored red in the electronic version) and 10 GeV to 100 GeV (dashed line colored blue). The solid gray regions represent the detection threshold assuming the sensitivity improves from 2 to 10 years by the square root of the exposure (top edge) and linearly with exposure (bottom edge). The lower plot shows the factor increase in sensitivity. For small extended sources, our detection threshold to the extension of a source will improve by a factor larger than the square root of the exposure.
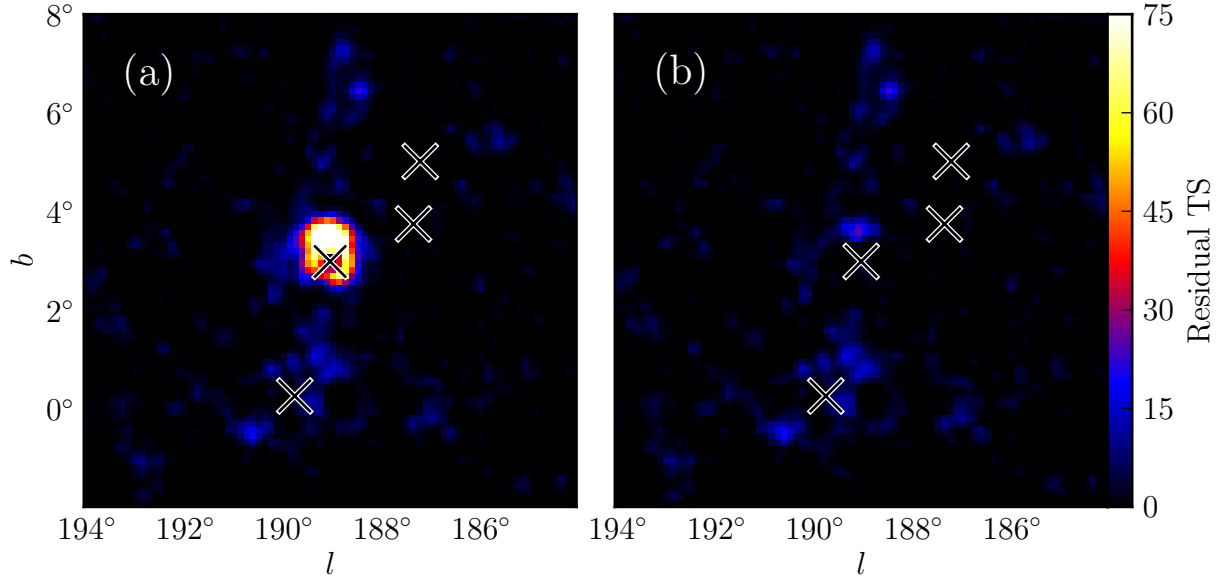
Fig. 7.— A test statistic map generated for the region around the SNR IC443 using photons with energies between 1 GeV and 100 GeV. (a) test statistic map after subtracting IC443 modeled as a point-like source. (b) same as (a), but IC443 modeled as extended source. Crosses represent sources included in the model of the region.
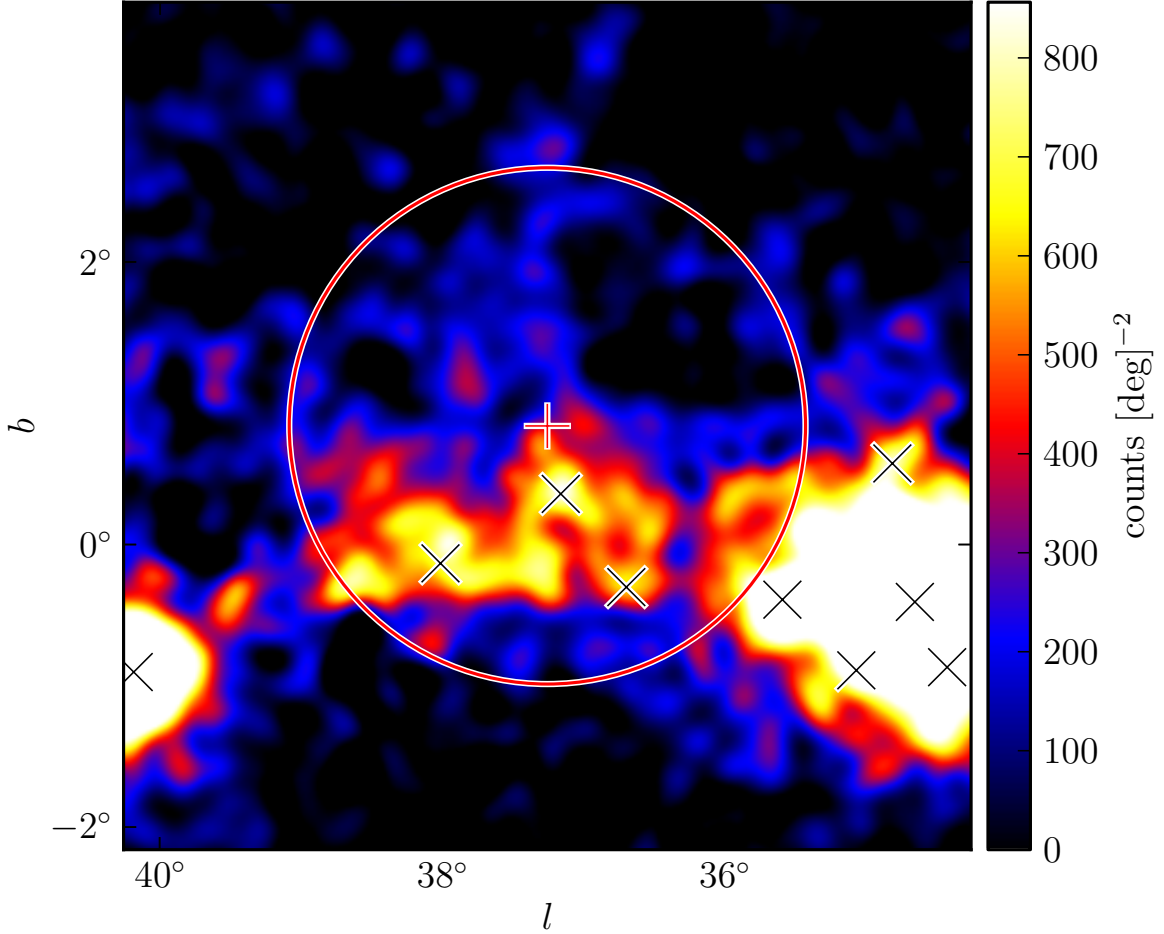
Fig. 8.— A diffuse-emission-subtracted 1 GeV to 100 GeV counts map of the region around 2FGL J1856.2+0450c smoothed by a 0°.1 2D Gaussian kernel. The plus-shaped marker and circle (colored red in the online version) represent the center and size of the best fit radially symmetric source with a uniform intensity profile. The black crosses represent the position of other 2FGL sources. The extension is statistically significant, but the extension encompasses many 2FGL sources and the emission does not look to be uniform. This source is probably fitting large-scale diffuse residual features. Although the fit is statistically significant, it likely corresponds to residual features of inaccurately modeled diffuse emission picked up by the fit. We manually discard candidates that appear like this.

Table 3. Analysis of the twelve extended sources included in 2FGL

Name	GLON (deg.)	GLAT (deg.)	σ (deg.)	TS	TS_{ext}	Pos Err (deg.)	Flux[a] (ph cm^{-2} s^{-1})	Index
			E>1 GeV					
SMC	302.68	-44.81	$1.75 \pm 0.07 \pm 0.02$	94.8	67.4	0.12	3.3 ± 0.4	2.41 ± 0.17
LMC	279.10	-32.61	$1.74 \pm 0.05 \pm 0.13$	1101.3	860.5	0.05	15.5 ± 0.6	2.48 ± 0.06
IC443	189.05	3.04	$0.36 \pm 0.01 \pm 0.04$	10719.8	510.4	0.01	64.8 ± 1.2	2.23 ± 0.02
Vela X	263.34	-3.11	0.88					
Centarus A	309.52	19.42	~ 10					
W28	6.50	-0.27	$0.43 \pm 0.02 \pm 0.03$	1324.8	177.4	0.01	58.0 ± 1.8	2.63 ± 0.03
W30	8.61	-0.20	$0.36 \pm 0.02 \pm 0.02$	465.4	73.3	0.02	30.7 ± 1.6	2.59 ± 0.04
W44	34.69	-0.38	$0.36 \pm 0.01 \pm 0.02$	1903.3	217.7	0.01	73.6 ± 1.8	2.68 ± 0.02
W51C	49.13	-0.45	$0.28 \pm 0.02 \pm 0.05$	1819.5	115.7	0.01	39.3 ± 1.3	2.35 ± 0.03
Cygnus Loop	74.22	-8.46	$1.72 \pm 0.05 \pm 0.07$	356.5	356.5	0.06	11.1 ± 0.7	2.53 ± 0.11
			E>10 GeV					
MSH 15−52	320.38	-1.22	$0.20 \pm 0.04 \pm 0.03$	76.2	6.5	0.03	0.6 ± 0.7	2.27 ± 0.73
HESS J1825−137	17.56	-0.46	$0.65 \pm 0.03 \pm 0.01$	83.6	55.9	0.05	1.8 ± 0.2	1.74 ± 0.19

[a]Integrated in the fit energy range (either 1 GeV 100 GeV or 10 GeV 100 GeV).

Note. — All sources were fit using a spatial model assuming a uniform radially symmetric intensity distribution. GLON and GLAT are Galactic longitude and latitude of the best fit extended source respectively. The first error on σ is statistical and the second is systematic (see Section 5.2). Pos Err is the error on the position of the source. Vela X and the Centarus A Lobes were not fit in our analysis but are include for completeness.
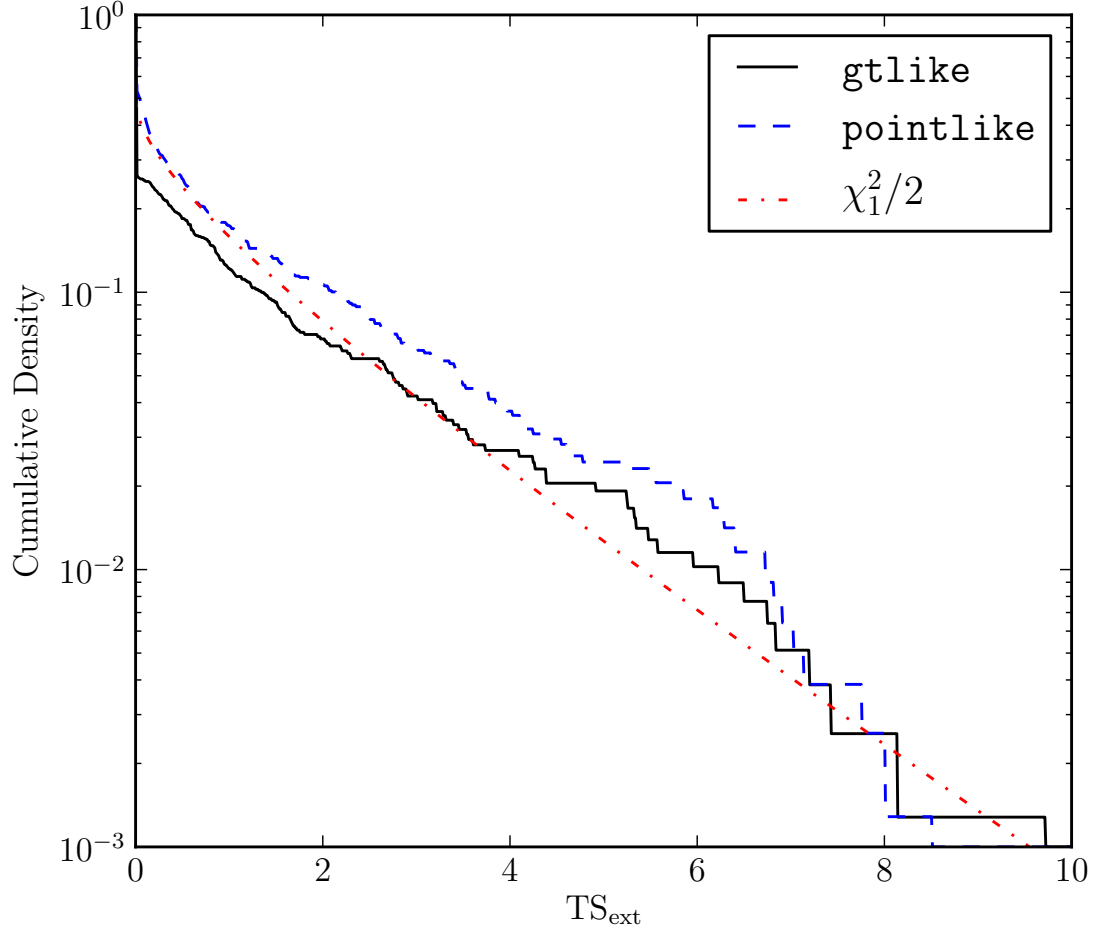
Fig. 9.— The cumulative density of TS_{ext} for the 783 clean AGN in 2LAC that were significant above 1 GeV calculated with `pointlike` (dashed line colored blue in the electronic version) and with `gtlike` (solid line colored red). AGN are too far and too small to be resolved by the LAT. Therefore, the cumulative density of TS_{ext} is expected to follow a $\chi^2/2$ distribution (Equation 9, the dash-dotted line colored red).

Table 4. Extension fit for the nine new extended sources

Name	GLON (deg.)	GLAT (deg.)	σ (deg.)	TS	TS$_{\mathrm{ext}}$	Pos Err (deg.)	Flux[a] (ph cm^{-2} s^{-1})	Index	Counterpart
				E>1 GeV					
2FGL J0823.0−4246	260.32	-3.28	$0.37 \pm 0.03 \pm 0.02$	320.9	46.3	0.02	8.5 ± 0.7	2.20 ± 0.09	Puppis A
2FGL J1627.0−2425c	353.08	16.78	$0.41 \pm 0.05 \pm 0.02$	144.5	31.1	0.04	6.5 ± 0.6	2.49 ± 0.14	Ophiuchus
2FGL J1712.4−3941	347.25	-0.54	$0.56 \pm 0.04 \pm 0.01$	75.0	39.6	0.05	4.2 ± 0.9	1.47 ± 0.12	RX J1713.7−3946
				E>10 GeV					
2FGL J0851.7−4635	266.29	-1.43	$1.13 \pm 0.08 \pm 0.05$	116.1	87.2	0.07	1.3 ± 0.2	1.76 ± 0.21	Vela Jr.
2FGL J1615.0−5051	332.38	-0.14	$0.33 \pm 0.04 \pm 0.01$	53.4	16.3	0.04	1.1 ± 0.2	2.24 ± 0.28	HESS J1616−508
2FGL J1615.2−5138	331.66	-0.66	$0.42 \pm 0.03 \pm 0.01$	76.6	48.0	0.05	1.2 ± 0.2	1.77 ± 0.24	HESS J1614−518
2FGL J1632.4−4753c	336.41	0.22	$0.44 \pm 0.04 \pm 0.03$	127.8	64.5	0.04	1.9 ± 0.2	2.29 ± 0.21	HESS J1632−478
2FGL J1837.3−0700c	25.08	0.13	$0.35 \pm 0.08 \pm 0.03$	46.2	18.8	0.07	1.0 ± 0.2	1.63 ± 0.29	HESS J1837−069
2FGL J2021.5+4026	78.18	2.19	$0.59 \pm 0.03 \pm 0.02$	222.2	116.4	0.04	1.8 ± 0.2	2.31 ± 0.19	γ-Cygni

[a]Integrated in the fit energy range (either 1 GeV to 100 GeV or 10 GeV 100 GeV).

Note. — The columns in this table have the same meaning as those in Table 3.

Table 5. Dual localization, alternative PSF, and alternative diffuse results

Name	$\mathrm{TS}_{\texttt{pointlike}}$	$\mathrm{TS}_{\texttt{gtlike}}$	$\mathrm{TS}_{\mathrm{alt,diff}}$	$\mathrm{TS}_{\mathrm{ext}\,\texttt{pointlike}}$	$\mathrm{TS}_{\mathrm{ext}\,\texttt{gtlike}}$	$\mathrm{TS}_{\mathrm{ext\,alt,diff}}$	σ (deg.)	$\sigma_{\mathrm{alt,diff}}$ (deg.)	$\sigma_{\mathrm{alt,psf}}$ (deg.)	$\mathrm{TS}_{\mathrm{inc}}$
				E>1 GeV						
2FGL J0823.0−4246	350.9	320.9	352.5	66.0	46.3	53.6	0.37	0.39	0.38	22.1
2FGL J1627.0−2425c	170.2	144.5	112.6	43.9	31.1	23.9	0.41	0.40	0.39	20.0
2FGL J1712.4−3941	80.9	75.0	43.4	47.4	39.6	22.2	0.56	0.56	0.54	6.4
				E>10 GeV						
2FGL J0851.7−4635	116.7	116.1	122.3	87.1	87.2	90.4	1.13	1.16	1.17	16.1
2FGL J1615.0−5051	52.4	53.4	55.6	17.5	16.3	17.4	0.33	0.32	0.32	11.9
2FGL J1615.2−5138	76.3	76.6	86.3	44.0	48.0	52.6	0.42	0.43	0.43	37.0
2FGL J1632.4−4753c	126.6	127.8	120.7	63.9	64.5	64.1	0.44	0.44	0.47	40.6
2FGL J1837.3−0700c	45.4	46.2	39.0	18.5	18.8	16.6	0.35	0.34	0.38	12.6
2FGL J2021.5+4026	234.3	222.2	235.6	135.9	116.4	121.4	0.59	0.60	0.60	24.3

Note. — $\mathrm{TS}_{\texttt{pointlike}}$, $\mathrm{TS}_{\texttt{gtlike}}$, and $\mathrm{TS}_{\mathrm{alt,diff}}$ are the test statistic values from `pointlike`, `gtlike`, and `gtlike` with the alternate diffuse model respectively. $\mathrm{TS}_{\mathrm{ext}\,\texttt{pointlike}}$, $\mathrm{TS}_{\mathrm{ext}\,\texttt{gtlike}}$, and $\mathrm{TS}_{\mathrm{ext\,alt,diff}}$ are the test statistic values of the extension test from `pointlike`, `gtlike`, and `gtlike` with the alternate diffuse model respectively. σ, $\sigma_{\mathrm{alt,diff}}$, and $\sigma_{\mathrm{alt,psf}}$ are the fit extension with the standard analysis, the alternate diffuse model, and the alternate PSF respectively. $\mathrm{TS}_{\mathrm{inc}}$ is the test statistic for the two point-like source hypothesis test (see Section 2.4).
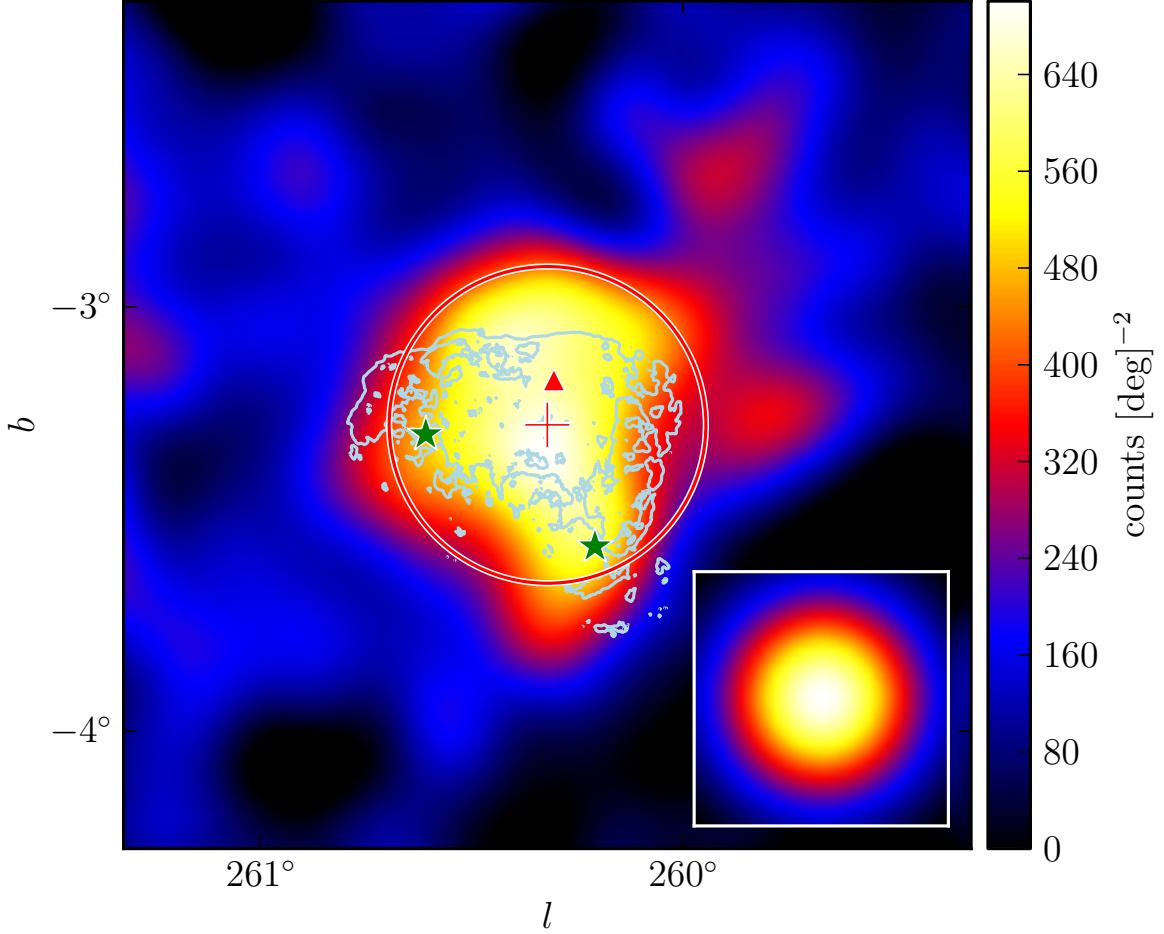
Fig. 10.— A diffuse-emission-subtracted 1 GeV to 100 GeV counts map of 2FGL J0823.0−4246 smoothed by a 0°.1 2D Gaussian kernel. The triangular marker (colored red in the online version) represents the 2FGL position of this source. The plus-shaped marker and the circle (colored red) represent the best fit position and extension of this source assuming a radially symmetric uniform surface brightness. The two star-shaped markers (colored green) represent 2FGL sources that were removed from the background model. The lower right inset is the model predicted emission from a point-like source with the same spectrum as 2FGL J0823.4−4305 smoothed by the same kernel. This source is spatially coincident with the Puppis A SNR. The light blue contours correspond to the X-ray image of Puppis A observed by *ROSAT* (Petre et al. 1996).
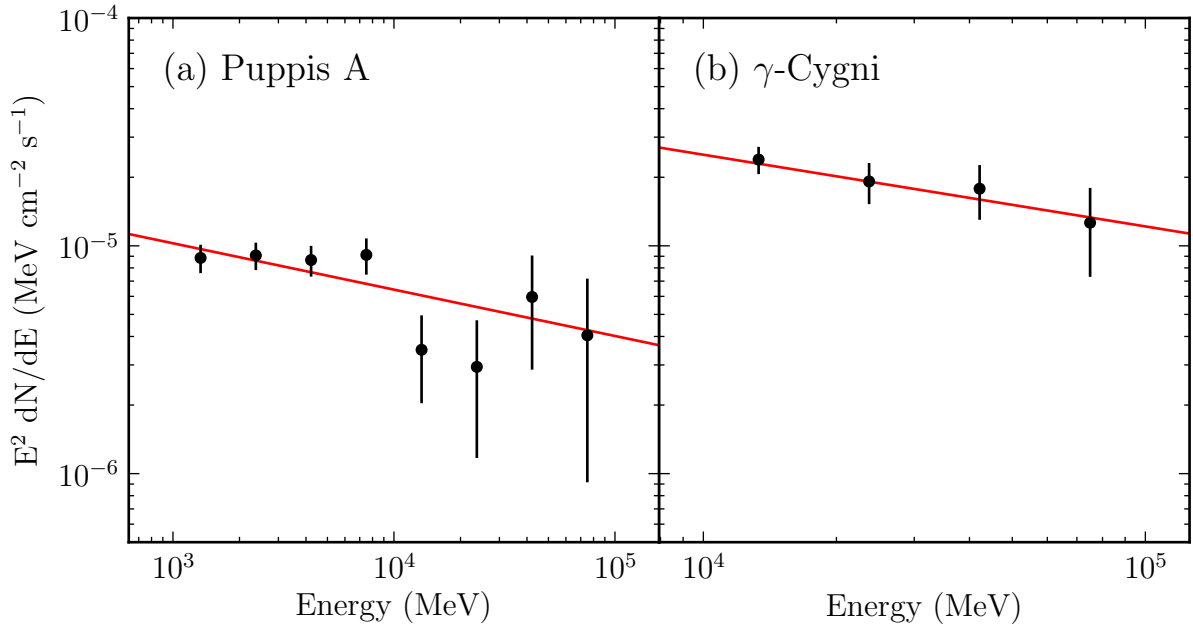
Fig. 11.— The spectral energy distribution of the extended sources Puppis A (2FGL J0823.0−4246) and γ-Cygni (2FGL J2021.5+4026). The lines (colored red in the online version) are the best fit power-law spectral models of these sources. The spectral errors are statistical only.
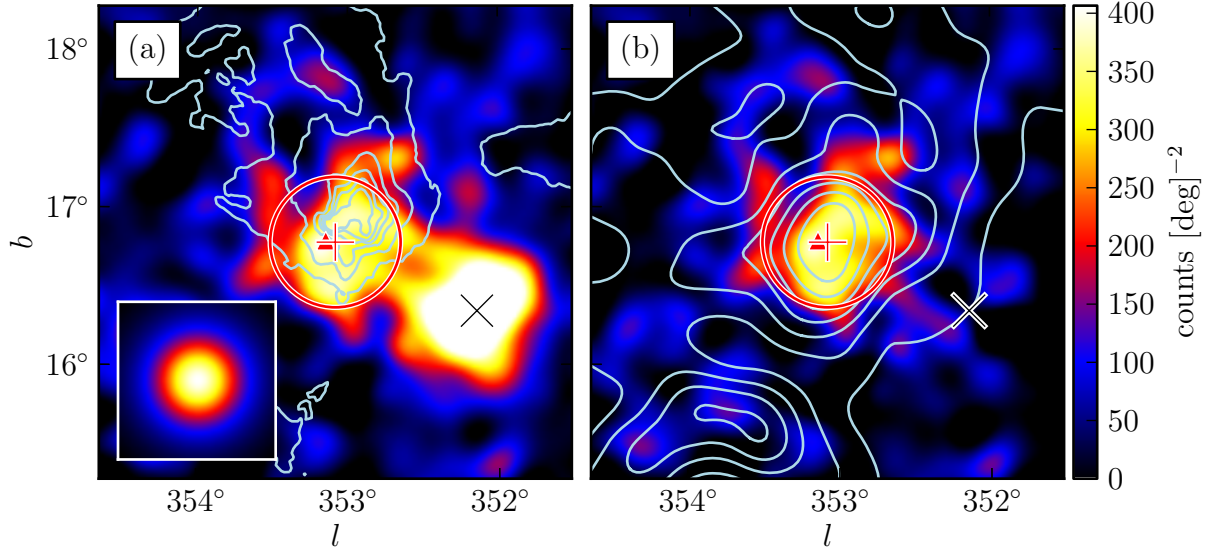
Fig. 12.— A diffuse-emission-subtracted 1 GeV to 100 GeV counts map of (a) the region around 2FGL J1627.0−2425 smoothed by a 0°.1 2D Gaussian kernel (b) also the emission from 2FGL J1625.7−2526 subtracted. The triangular marker (colored red in the online version) represents the 2FGL position of this source. The plus-shaped marker and the circle (colored red) represent the best fit position and extension of this source assuming a radially symmetric uniform surface brightness. The contours in (a) correspond to the 100 micrometer image observed by IRAS (Young et al. 1986). The contours in (b) correspond to ^{12}CO ($J = 1 \to 0$) emission integrated from -8 km/s to 20 km/s. They are from de Geus et al. (1990), were cleaned using the moment-masking technique (Dame 2011), and have been smoothed by a 0°.25 2D Gaussian kernel.
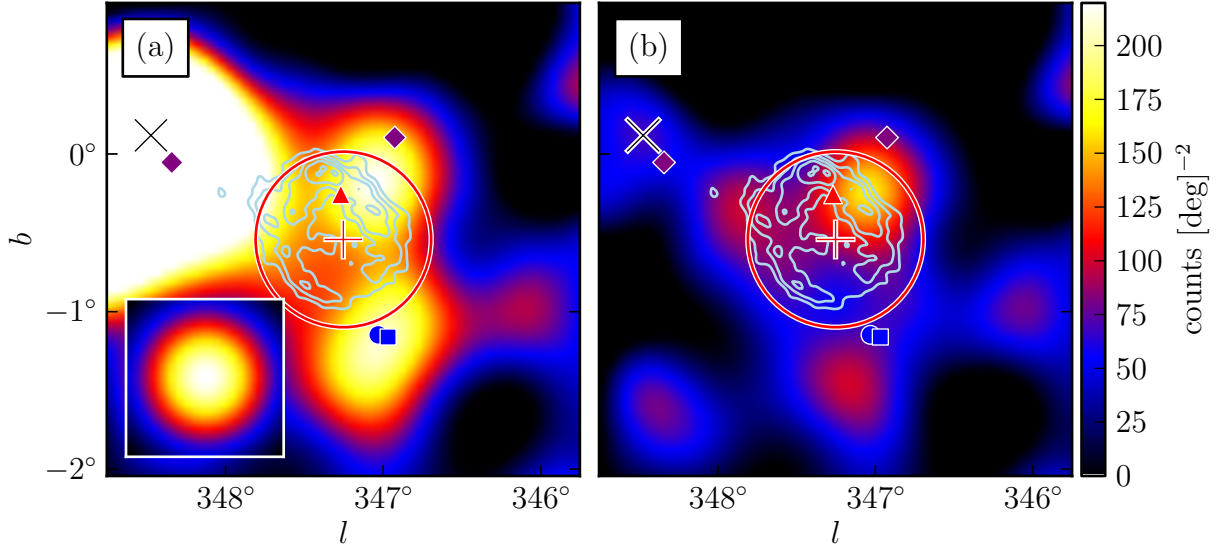
Fig. 13.— A diffuse-emission-subtracted 1 GeV to 100 GeV counts map of 2FGL J1712.4−3941 (a) smoothed by a 0°.25 2D Gaussian kernel and (b) with the emission from the background sources subtracted. This source is spatially coincident with RX J1713.7−3946 and was recently studied in Abdo et al. (2011c). The triangular marker (colored red in the online version) represents the 2FGL position of this source. The plus-shaped marker and the circle (colored red) are the best fit position and extension of this source assuming a radially symmetric uniform surface brightness. The contours (colored light blue) correspond to the TeV image (Aharonian et al. 2007b). The region was analyzed with the same background model as Abdo et al. (2011c). Source A is coincident with 2FGL J1715.4−4024c and the circular and square-shaped marker (colored blue) represent the 2FGL and relocalized position of this source respectively. The diamond-shaped markers (colored purple) represent the position of source B and C that were added to the background model.
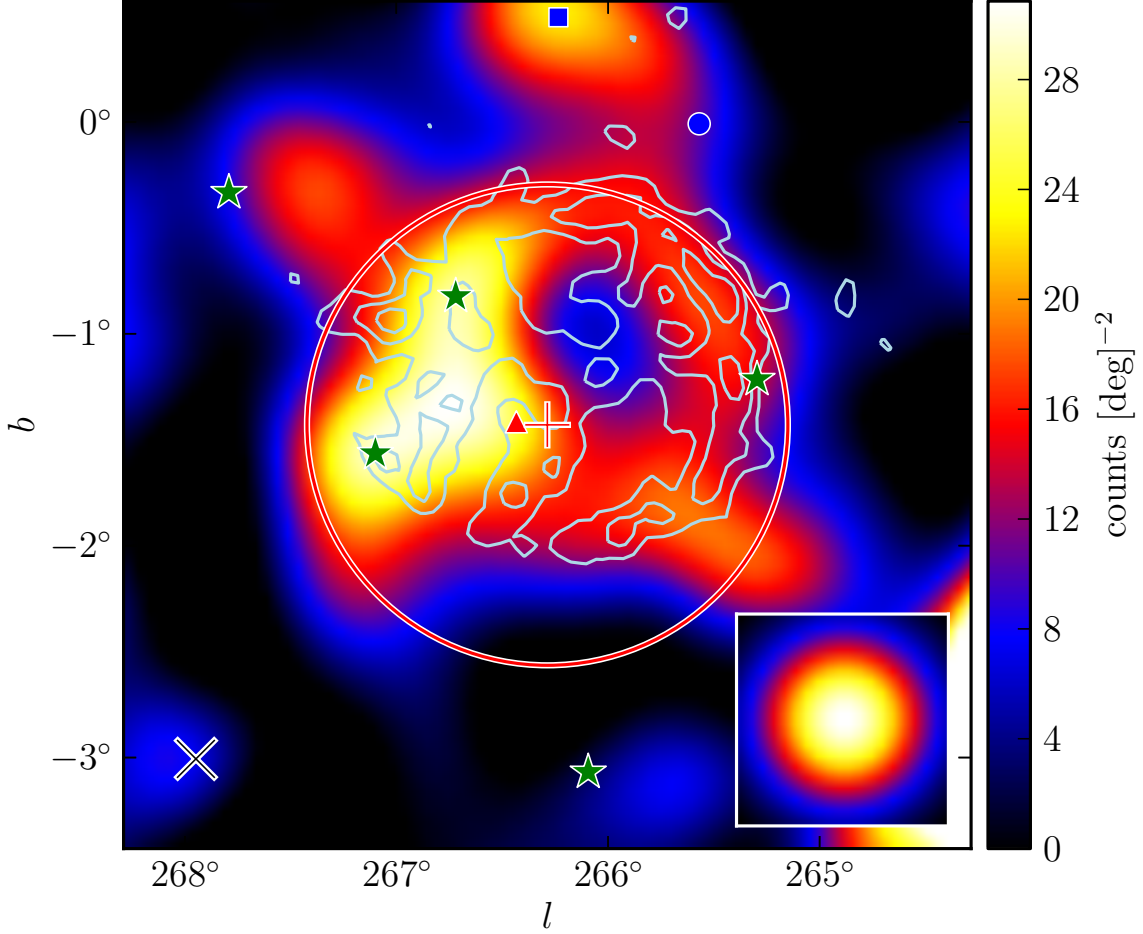
Fig. 14.— A diffuse-emission-subtracted 10 GeV to 100 GeV counts map of 2FGL J0851.7−4635 smoothed by a 0°.25 2D Gaussian kernel. The triangular marker (colored red in the electronic version) represents the 2FGL position of this source. The plus-shaped marker and the circle (colored red) are the best fit position and extension of this source assuming a radially symmetric uniform surface brightness. The five star-shaped markers (colored green) represent 2FGL sources that were removed from the background model. The circular and square marker (colored blue) represents the 2FGL and relocalized position of 2FGL J0854.7−4501 respectively. This extended source is spatially coincident with the Vela Jr. SNR. The contours (colored light blue) correspond to the TeV image of Vela Jr. (Aharonian et al. 2007a).
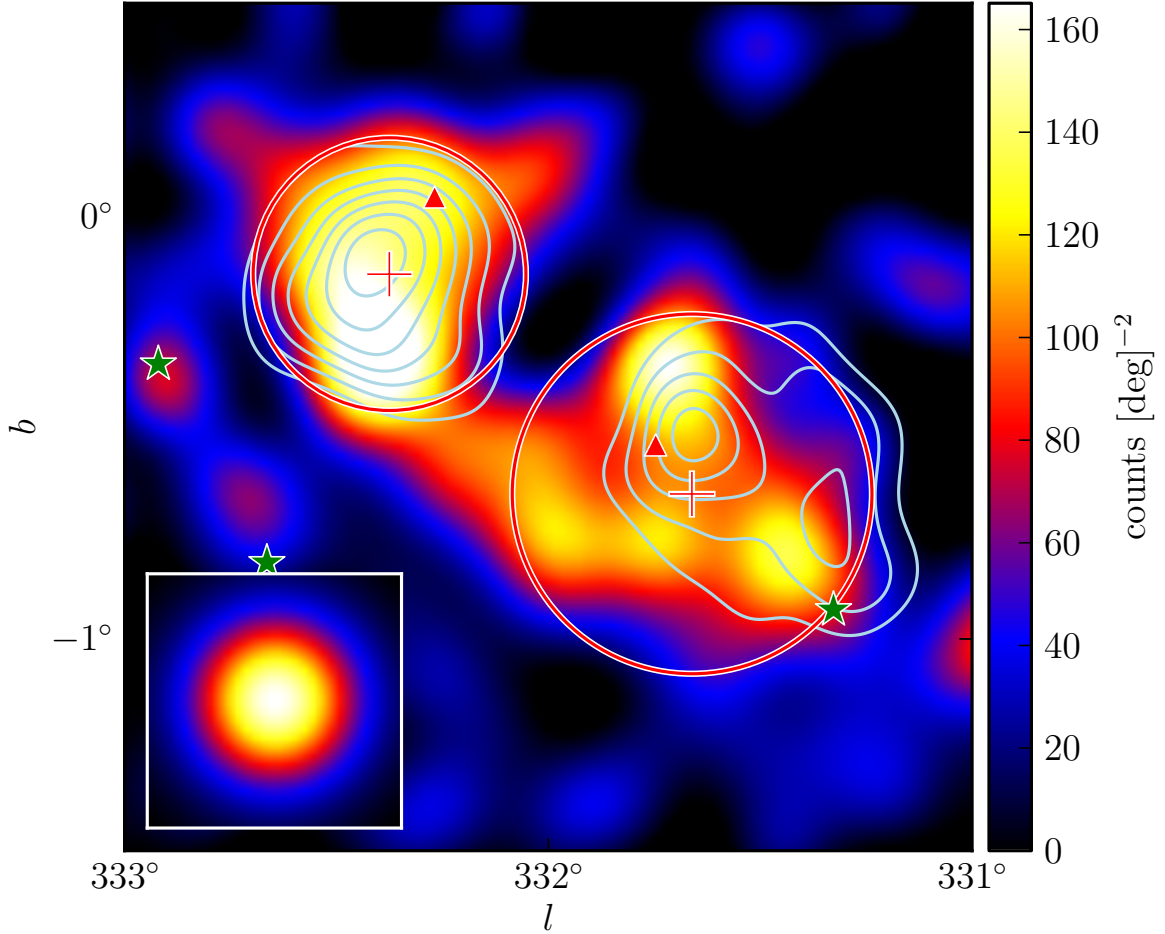
Fig. 15.— A diffuse-emission-subtracted 10 GeV to 100 GeV counts map of 2FGL J1615.0−5051 (upper left) and 2FGL J1615.2−5138 (lower right) smoothed by a 0°.1 2D Gaussian kernel. The triangular markers (colored red in the electronic version) represent the 2FGL positions of these sources. The cross-shaped markers and the circles (colored red) represent the best fit positions and extensions of these sources assuming a radially symmetric uniform surface brightness. The three star-shaped markers (colored green) represent 2FGL sources that were removed from the background model. The contours (colored light blue) correspond to the TeV image of HESS J1616−508 (left) and HESS J1614−518 (right) (Aharonian et al. 2006).
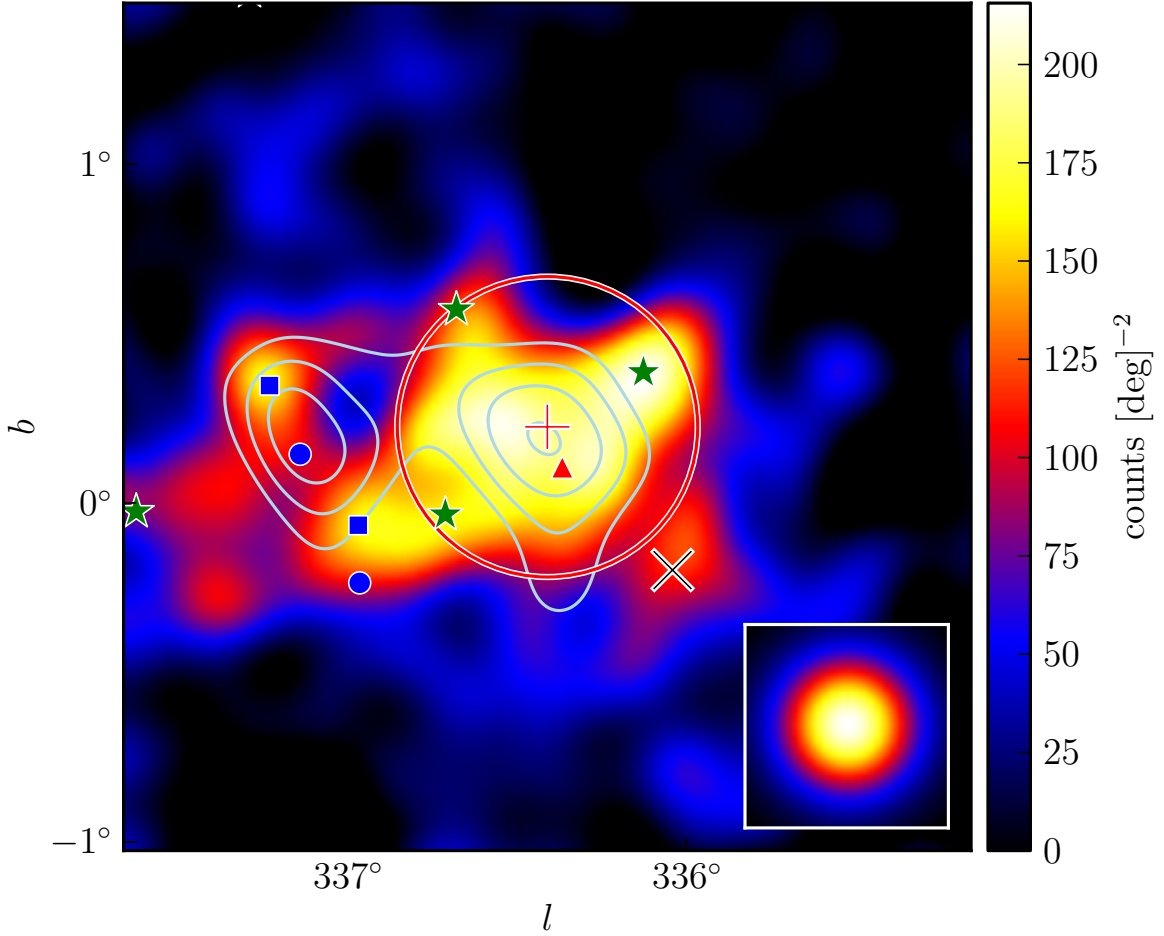
Fig. 16.— A diffuse-emission-subtracted 10 GeV to 100 GeV counts map of 2FGL J1632.4−4753c smoothed by a 0°.1 2D Gaussian kernel. The triangular marker (colored red in the electronic version) represents the 2FGL position of this source. The plus-shaped marker and the circle (colored red) are the best fit position and extension of 2FGL J1632.4−4753c assuming a radially symmetric uniform surface brightness. The four star-shaped markers (colored green) represent 2FGL sources that were removed from the background model. The circular and square markers (colored blue) represent the 2FGL and relocalized positions respectively of 2FGL J1635.4−4717c (left) and 2FGL J1636.3−4740c (right). The contours (colored light blue) correspond to the TeV image of HESS J1632-478 (Aharonian et al. 2006).
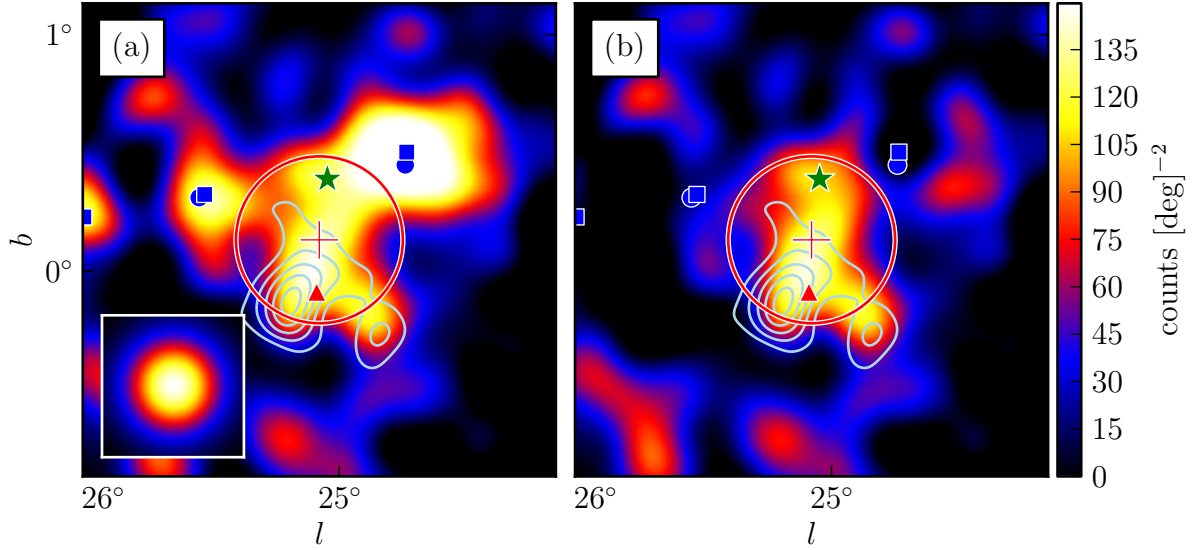
Fig. 17.— A diffuse-emission-subtracted 10 GeV to 100 GeV counts map of the region around 2FGL J1837.3−0700c (a) smoothed by a 0°.1 2D Gaussian kernel and (b) with the emission from the background sources subtracted. The triangular marker (colored red in the online version) represents the 2FGL position of this source. The plus-shaped marker and the circle (colored red) represent the best fit position and extension of 2FGL J1837.3−0700c assuming a radially symmetric uniform surface brightness. The circular and square markers (colored blue) represent the 2FGL and the relocalized position of 2FGL J1839.3−0558c (left), 2FGL J1836.8−0623c (middle), and 2FGL J1834.7−0705c (right). The star-shaped marker (colored green) represent a 2FGL source that was removed from the background model. The contours (colored light blue) correspond to the TeV image of HESS J1837−069 (Aharonian et al. 2006).
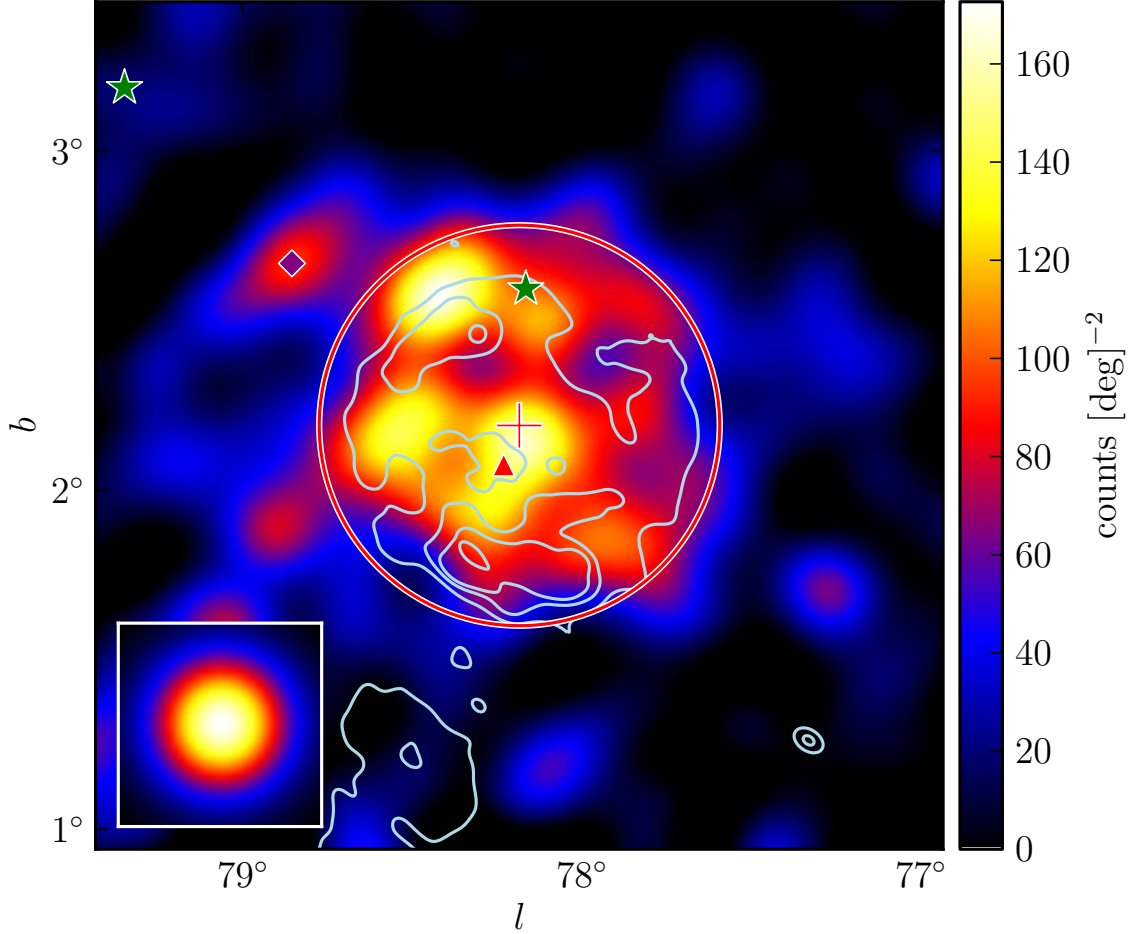
Fig. 18.— A Diffuse-emission-subtracted subtracted 10 GeV to 100 GeV counts map of the region around 2FGL J2021.5+4026 smoothed by a 0°.1 2D Gaussian kernel. The triangular marker (colored red in the online version) represents the 2FGL position of this source. The plus-shaped marker and the circle (colored red) represent the best fit position and extension of 2FGL J2021.5+4026 assuming a radially symmetric uniform surface brightness. The star-shaped markers (colored green) represent 2FGL sources that were removed from the background model. The diamond-shaped marker (colored purple) represents the position of a source not in 2FGL that was added to the region. 2FGL J2021.5+4026 is spatially coincident with the γ-Cygni SNR. The contours (colored light blue) correspond to the 408MHz image of γ-Cygni observed by the Canadian Galactic Plane Survey.
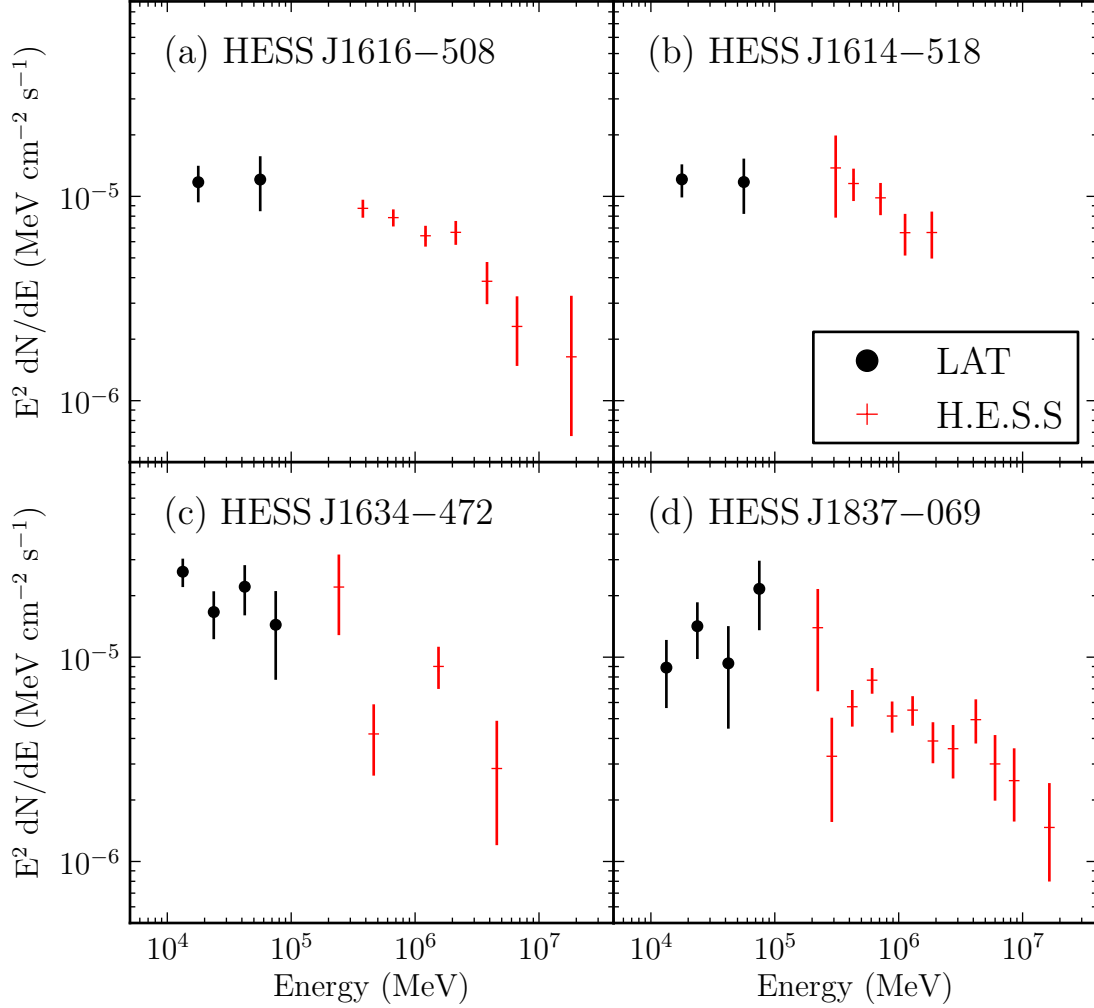
Fig. 19.— The spectral energy distribution of four extended sources associated with unidentified extended TeV sources. The black points with circular markers are obtained by the LAT. The points with plus-shaped markers (colored red in the electronic version) are for the associated H.E.S.S. sources. (a) the LAT SED of 2FGL J1615.0−5051 together with the H.E.S.S. SED of HESS J1616−508. (b) 2FGL J1615.2−5138 and HESS J1614−518. (c) 2FGL J1632.4−4753c and HESS J1632−478. (d) 2FGL J1837.3−0700c and HESS J1837−069. The H.E.S.S. data points are from (Aharonian et al. 2006). Both LAT and H.E.S.S. spectral errors are statistical only.
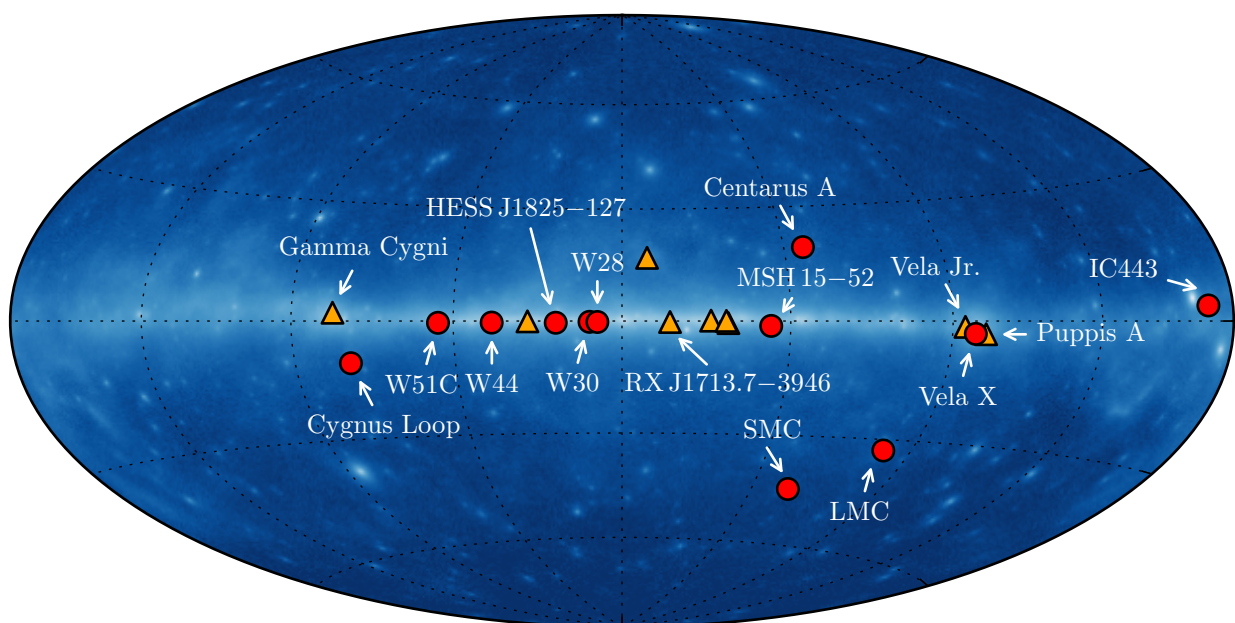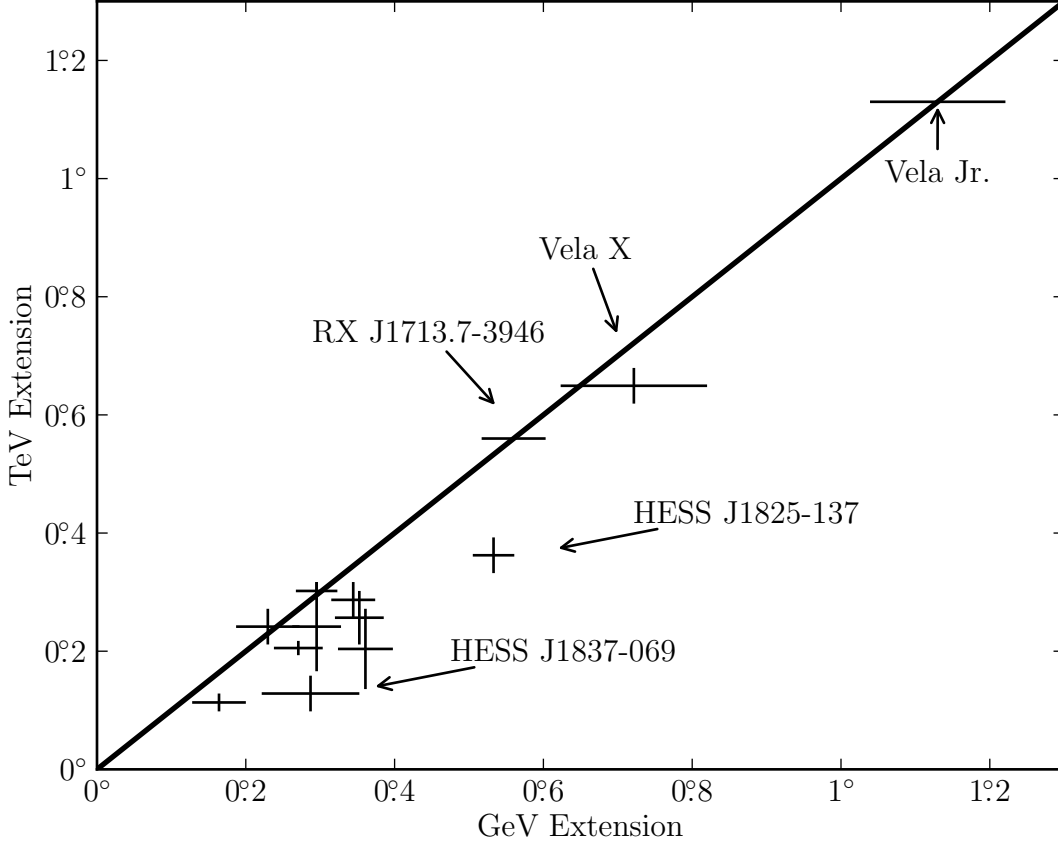
Fig. 20.— The 21 spatially extended sources detected by the LAT at GeV energies with two years of data. The twelve extended sources included in 2FGL are represented by the circular markers (colored red in the online version). The nine new extended sources are represented by the triangular markers (colored orange).

Fig. 21.— A comparison of the size of extended sources detected at both GeV and TeV energies. The TeV size of W30, 2FGL J1837.3−0700c, 2FGL J1632.4−4753c, 2FGL J1615.0−5051, and 2FGL J1615.2−5138 are from Aharonian et al. (2006). The TeV size of MSH 15−52, HESS J1825−137, Vela X, Vela Jr., RX J1713.7−3946 and W28 are from Aharonian et al. (2005, 2006b,c, 2007a,b, 2008). The TeV size of IC443 is from Acciari et al. (2009) and W51c is from Krause et al. (2011). The TeV size of MSH 15−52, HESS J1614−518, HESS J1632−478, and HESS J1837−069 have only been reported with an elliptical 2D Gaussian fit and so the assumed size is the average of the semi-major and semi-minor axis. The LAT extension of Vela X is from Abdo et al. (2010f). Except for RX J1713.7−3946 and Vela Jr., the TeV sources were fit assuming a 2D Gaussian surface brightness so the plotted GeV and TeV extensions were first converted to r_{68} (see Section 2.5). Because of their large size, the shape of RX J1713.7−3946 and Vela Jr. were not directly fit at TeV energies. Here, we take their sizes to be the same as the LAT size and do not converted them to r_{68}. The LAT extension errors are the statistical and systematic errors added in quadrature.
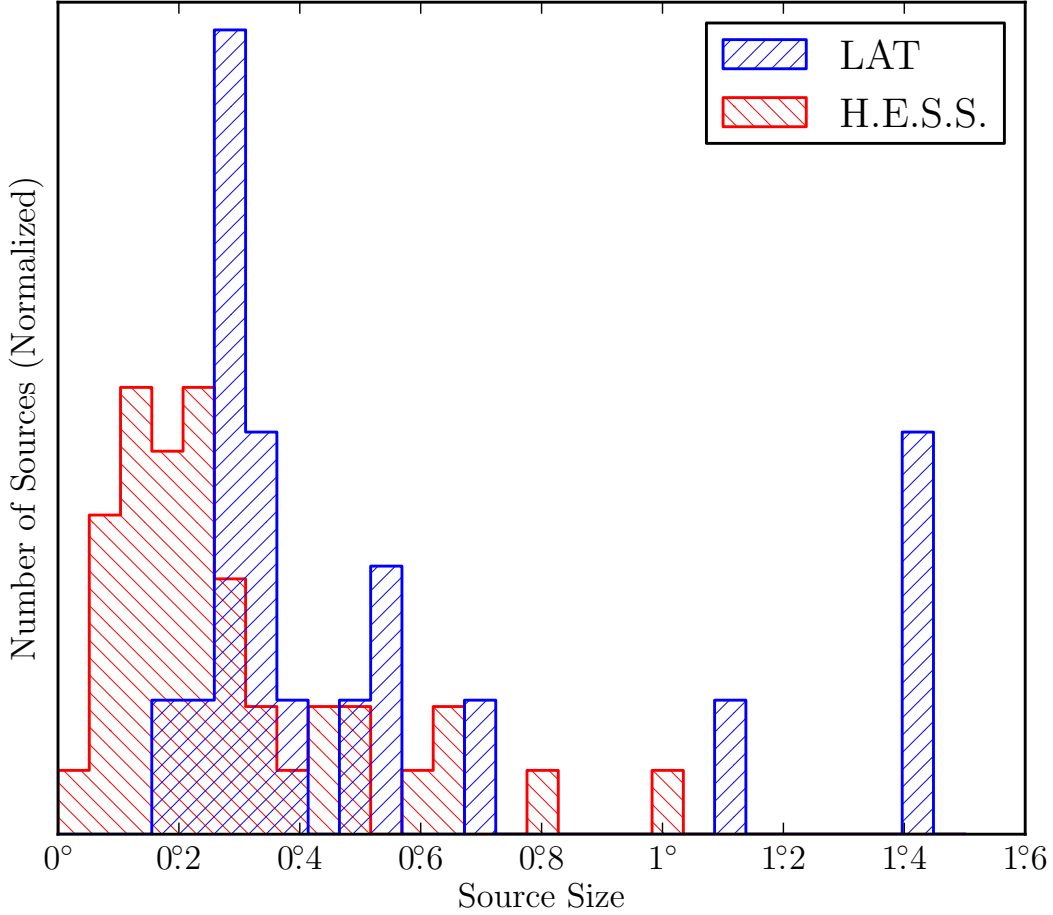
Fig. 22.— The distribution of the size of the 22 extended LAT sources at GeV energies (colored blue in the electronic version) and the size of the 42 extended H.E.S.S. sources at TeV energies (colored red). The size of Vela X is taken from Abdo et al. (2010f). Except for RX J1713.7−3946 and Vela Jr., the H.E.S.S. sources were fit with a 2D Gaussian surface brightness model so the LAT and H.E.S.S. sizes are first converted to r_{68}. Because the spatial morphology of RX J1713.7−3946 and Vela Jr. is poorly described by a 2D Gaussian surface brightness model, the GeV and TeV extensions are included assuming a uniform surface brightness model.
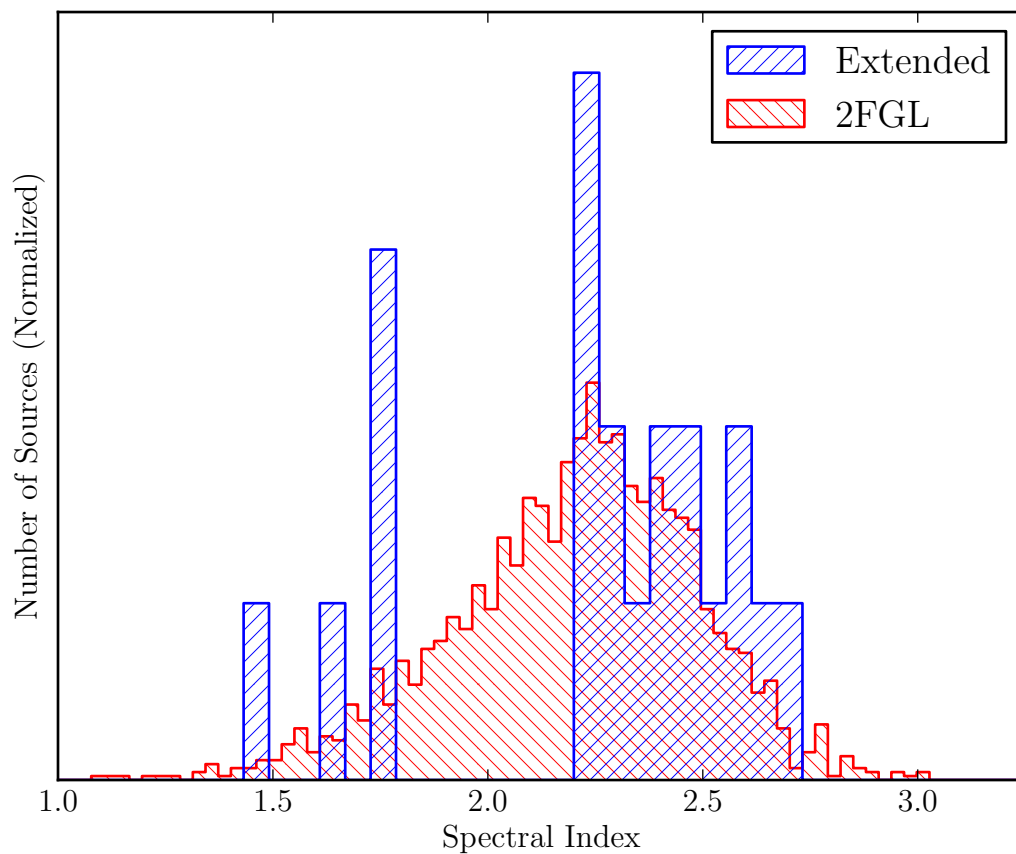
Fig. 23.— The distribution of spectral indices of the 1873 2FGL sources (colored red in the electronic version) and the 21 spatially extended sources (colored blue). The index of Centarus A is taken from Abdo et al. (2011b) and the index of Vela X is taken from Abdo et al. (2010f).